CHAPTER 5 : THE VELOCITY FIELD UPSTREAM FOR THE ORIFICE FLOW OF A POLYMER SOLUTION.

5.1. Introduction

As it has already been stressed previously, contraction flows have received considerable attention by various authors. They are encountered in many industrial applications involving polymer melts and solutions. They are also of a great scientific interest, because they involve both shear and extension and they serve as excellent problems for the numerical simulation of non-Newtonian flows.

The dominance of shear or extension in such flows depends on the contraction ratio, the flow regime and, of course, on material properties. The nature of the fluid is a very important parameter and the flow pattern varies enormously depending on whether the fluid is Newtonian or shear-thinning, whether it is elastic or inelastic, etc. But, in general, extension is dominant in the central flow core region whereas shear dominates at the wall, on the corners of the contraction as well as far upstream the contraction.

The knowledge of the velocity distribution is essential for the good comprehension of such flows. Collins and Schowalter [1], determined the behavior of a power-law fluid in the entry region by applying boundary layer theory principles. They provided estimates of the shape of the velocity profile as a function of the power-law index.

For a shear-thinning power-law fluid flowing through a tube of circular section, the velocity field is :

$$U_z(r) = \frac{(3n+1)\,Q}{(n+1)\,\pi R^2}\left\{1 - \left[\frac{r}{R}\right]^{1+\frac{1}{n}}\right\} \qquad (5.1)$$

where the cylindrical polar coordinates (r, θ, z) are considered and z is the flow direction. Q is the flow rate, R is the tube radius and n is the power-law index.

Cogswell [2] and later Binding [3], in their analyses of the contraction flow of power-law liquids, assumed that, in such flows, the distribution of the velocity component in the flow direction would be approximately that of eq. (5.1). Sufficiently far upstream, R would be equal to the upstream tube radius and near the contraction plane it would be the radius of the envelope of the fluid that will pass through the contraction R= R(z). Binding showed that if eq. (5.1) is valid, then the continuity equation can be used to derive the radial velocity component :

$$U_r(r) = \frac{(3n+1)\,Q\,r}{(n+1)\,\pi\,R^3}\left\{1 - \left[\frac{r}{R}\right]^{1+\frac{1}{n}}\right\}\frac{dR}{dz} \qquad (5.2)$$

The structure of the upstream field implies also :

$$U_\theta = 0 \qquad (5.3)$$

Many authors provided experimental measurements of the velocity in contraction flows. Brocklebank and Smith [4] used stroboscopic streak-line photographs for velocity measurements and deduced the entry length in a pipe. The same technique was used by Boger and Ramamurthy [5, 6] who determined centerline profiles and developing profiles of the axial component for Methocel and Separan solutions. They found uniform profiles at the entrance for $0.585 < n < 1$ and for relatively high Reynolds numbers ($20 < Re < 1942$). They also verified the theoretical commonly accepted value (ex. [1, 19]) for the entry length L_e :

$$\frac{L_e}{R} = 0.122\,Re \qquad (5.4)$$

for $1 < Re < 1500$.

Cable and Boger [7] used the same method to study the velocity field in stable flow of viscoelastic aqueous Separan solutions. They found significant qualitative differences between velocity profiles in the vortex growth and divergent flow regimes which they have observed. During the vortex growth regime the axial profile overdeveloped even before the detachment plane of the vortices. In the vortex region it relaxed back to become fully developed downstream.

Binnington et al [8] provided profiles on the axis for a dilute Separan solution in a 4:1 contraction, obtained by the help of speckle imaging pictures. They showed that this profile started to differ from the Newtonian one above a critical value of the shear rate.

The Laser Doppler Velocimetry technique has proven to be a very helpful tool for the determination of the velocity fields of transparent polymeric liquids. Busby and McSporran [9] used a Laser anemometry technique (1976) in a flow of an aqueous 0.75% polyacrylamide (PAA) solution into a re-entrant tube geometry at Reynolds numbers in the range 100-500. They found that the major velocity rearrangements occurred only a few diameters upstream and downstream though a much longer distance was necessary for fully developed downstream conditions. They also found that the velocity varied in an oscillatory manner with the axial distance from the entry plane. Finally, their calculations of the "time of flight" along the central streamline confirmed

that the major rearrangements suffered by the fluid occurred during a time period short enough for memory effects to become significant.

This technique has been developed more in the last fifteen years and much better set-ups have been used. Ramamurthy and McAdam [10] presented LDA measurements on the entry region of a capillary rheometer. They confirmed the results of Cable and Boger showing that flow instabilities begin above the critical value of 0.03 for the Weissenberg number.

Hasegawa and Iwaida [11] found nearly constant stretch rates $\dot{\varepsilon}$ at the vortex region of an orifice flow of dilute polyoxyethylene (PEO) solutions. This value of the stretch rate was such that : $\dot{\varepsilon}\, t_{rel} = 0.5$, where t_{rel} is the generalized power-law Maxwell model relaxation time. They showed that the maximal value of the stretch rate may occur at a distance equal to many diameters upstream the contraction plane.

Xu et al. [12] and Wunderlich et al. [13] carried out LDA measurements on flows through planar contractions. Xu et al. tested a 3% solution of PDMS into a PDMS oil. Their results in a planar geometry are similar to those of Cable and Boger : deceleration in the axis during the divergent flow regime and off-center maxima. They have shown significant asymmetries in the flow due to slight asymmetries in the geometry.

Wunderlich et al. showed detailed profiles with off-center maxima and their development as one approaches to the contraction plane for very dilute (25 and 50 ppm) polyacrylamide (HPAM) solutions.

Lawler et al. [14] presented measurements of the variation of the velocity with time for a flow of a PAA solution. It varied periodically at regimes just before the appearance of the vortices, for Weissenberg numbers $0.8 < We < 1.2$. Similar quasi-sinusoidal periodicity of the velocity has been presented by McKinley et al. [15] with a polyisobutylene (PIB) solution. They have also presented off-center maxima in the divergent flow regime and a study of the influence of the contraction ratio on the vortex size and on the stability of the flow.

Raiford et al. [16] showed measurements on concentrated PIB solutions for various Reynolds and Weissenberg numbers. At high regimes the curve of the velocity profile of the axial component presented a discontinouity in the region of the flow axis : flow is proven to be divided into an accelerating core and an outer region where the flow retains its upstream profile.

In the present section we present LDA measurements on a contraction flow of a polyacrylamide (HPAM) solution of a very low concentration (100 ppm). It is a non shear-thinning solution in a thick solvent of glucose / water (described in an earlier section). The flow curve of this solution through the orifice of 1.2 mm has been previously determined [17, 18]. Our velocity measurements have been carried out at steady state conditions in the vortex growth regime.

The experimental set up for the orifice flow has been previously described (section 2.4.1). In section 5.2 we describe the LDA technique and in section 5.3 the experimental equipment used. The measurement techniques used to obtain both the axial and the radial components are presented in section 5.4. The results are given in section 5.5 and the conclusions in 5.6.

5.2. The Laser Doppler Velocimetry technique

5.2.1. The Doppler effect

The Laser Doppler Velocimetry (LDV) technique, is based on the optical Doppler effect. Let us consider a monochromatic light beam of frequency f_0 and wavelength λ_0 which is propagated following a direction represented by the unit vector $\vec{i_0}$ (Fig. 5.1) and a particle moving with a velocity $\vec{V}$, which is illuminated by this beam. This particle will diffuse light in all directions with a frequency f_d dependent on the observation angle in the following way:

$$f_d = f_0 + \frac{\vec{V}}{\lambda_0}\left(\vec{i_d} - \vec{i_0}\right) \qquad (5.5)$$

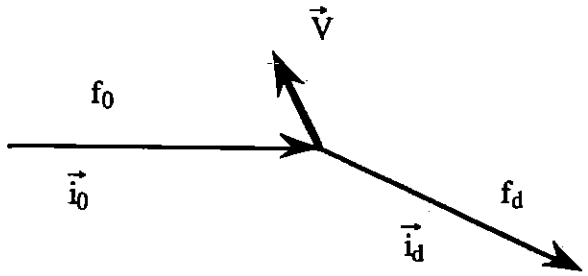

Figure 5.1.

The difference $f_D = f_d - f_0$, called the Doppler frequency, is thus proportional to the velocity of the particle. The relationship (5.5) is valid for light propagation in vacuum. In the case of a medium of a refraction index n, it is :

$$f_D = \frac{n\vec{V}}{\lambda_0}\left(\vec{i_d} - \vec{i_0}\right) \qquad (5.6)$$

In the case where the particle is simultaneously illuminated by two beams, it diffuses light coming from both beams (Fig. 5.2).

For any direction $\vec{i_k}$, the frequency of the light diffused relative to the first beam is :

$$f_1 = f_0 + \frac{\vec{V}}{\lambda_0}\left(\vec{i_k} - \vec{i_0}\right) \qquad (5.7)$$

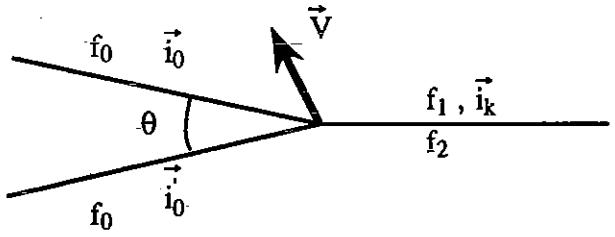

Figure 5.2.

and the light relative to the second one :

$$f_2 = f_0 + \frac{\vec{V}}{\lambda_0}\left(\vec{i_k} - \vec{i_0}\right) \qquad (5.8)$$

The composition of these two coherent light sources leads to a light with a Doppler frequency

$$f_D = f_2 - f_1 = \frac{\vec{V}}{\lambda_0}\left(\vec{i_0} - \vec{i_0}\right) \qquad (5.9)$$

Thus, this Doppler frequency is proportional to the component of the velocity of the particle that is perpendicular to the bisection of the angle θ which is formed by the incident beams $\vec{i_0}$ and $\vec{i_0}$:

$$f_D = \frac{2}{\lambda_0} \sin\frac{\theta}{2} V \qquad (5.10)$$

In this case the frequency does not depend on the direction of the observation, though this is not true for the intensity of the diffused light.

5.2.2. Laser Doppler Velocimetry with interference fringes.

The LDV technique with interference fringes is based on the principle that is described in the previous section. It is an optical non-invasive method of measuring the

velocity of a fluid by means of the light diffused by fine particles suspended on the fluid flow. It is thus necessary that the particles follow perfectly the flow.

A beam of monochromatic and coherent light is emitted from a laser source and it is splitted into two beams which are then converged. The point of the convergence of the two beams forms the measuring volume, an ellipsoid of revolution. A schematic representation of the intersection of this ellipsoid with the major plan of the measurements is shown in Fig. 5.3.

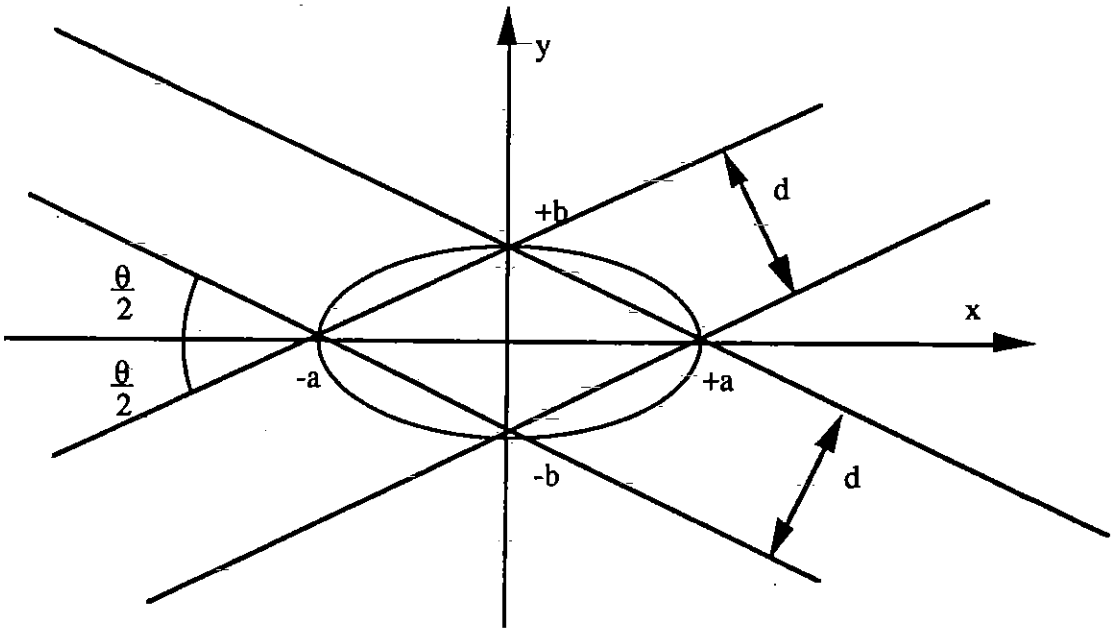

Figure 5.3.

The three dimensions of this ellipsoid are evidently the following :

$$2a = \frac{d}{\sin\frac{\theta}{2}} \quad (5.11) \qquad 2b = \frac{d}{\cos\frac{\theta}{2}} \quad (5.12) \qquad 2c = d \quad (5.13)$$

where d is the diameter of the beam in the convergence point. It is :

$$d = \frac{4 f \lambda}{\pi d_1} \qquad (5.14)$$

where: f is the focal distance of the convergent lens,

λ is the wavelength of the light beam in the medium of refraction index n, that is

$\lambda = \lambda_0/n$,

λ_0 is the wavelength in the air,

d_1 is the beam diameter as provided by the laser and

θ is the intersection angle of the beams in the medium.

The measuring volume is :

$$U \cong \frac{4}{3} \pi b^2 a \qquad (5.15)$$

since b and c are practically equal.

A network of fringes is developed in the ellipsoid consisting of a set of parallel planes alternatively dark and luminous. These planes are parallel to the bisection of the angle between the two beams and perpendicular to the plane formed by them. Each particle that passes through this network with a velocity $\vec{V}$ diffuses light only when traversing a luminous fringe. The diffused light is thus modulated with a frequency f_D proportional to the component of the velocity $\vec{V}$ which is perpendicular to the interference planes. Respecting the notation defined in Figure 5.4, the interfringe Δy is :

$$\Delta y = \frac{\lambda_0}{2 \sin \frac{\theta}{2}} \qquad (5.16)$$

and the Doppler frequency :

$$f_D = \frac{V_y}{\Delta y} = 2 \sin \frac{\theta}{2} \frac{V_y}{\lambda_0} \qquad (5.17)$$

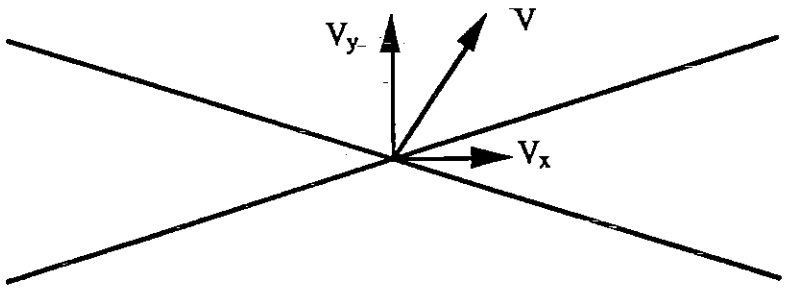

Figure 5.4.

The diffused light is collected by a photomultiplier which transforms it into an electric signal. This signal is treated in order to deduce the Doppler frequency and thus, the corresponding velocity component.

An ambiguity exists though as far as the sign of the measured velocity component is concerned : the same frequency may correspond to a positive or negative velocity component. This may introduce a source of error in a case where the velocity may take both positive and negative values. This might be for example the case in the vortex region of a polymer solution upstream an orifice.

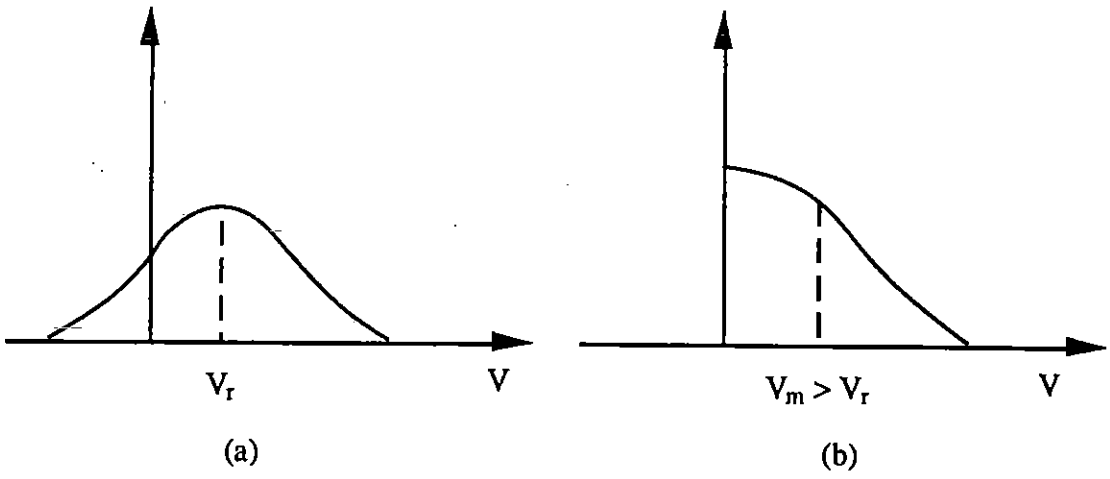

Figure 5.5.

Considering thus the histogram of Fig. 5.5.a, where both positive and negative values of the velocity exist, one can see that this histogram will be folded up and the resulting measured velocity V_m will be higher than the real one V_r (Fig. 5.5.b).

This error is avoided by increasing the light frequency by a constant very high value (40 MHz) which is considered later in the processing of the measurements. This is done by introducing a Bragg cell in the trajectory of one of the beams.

Another important point for the precision of the method is the ratio of the diameter of the particles to the interfringe Δy : the distribution of the intensity in the measuring volume depends on the position, since the intensity of the incident light is gaussian. The consequence of this is that the intensity of the light diffused by a particle depends on its position in the measuring volume. For a particle which has very small dimensions with respect to the interfringe, the diffusion of the light will follow the variation of the intensity in the network. On the other hand, for a particle of dimensions equal or higher than the interfringe the mean value of the intensity is practically constant and independent on its position. Thus, the particles should be big enough to avoid intensity dependence on the position on one hand, and small enough to ensure the fact that they will perfectly follow the flow on the other.

The quality of the Doppler signal depends also on the trajectory of the particle in the measuring volume as well as on the existence of eventual parasitic lights. The velocity gradients within the measuring volume play a very important role on the precision of the measurements.

5.3. The experimental equipment.

The experimental equipment is shown schematically in Fig. 5.6. A laser source provided a laser beam which was splitted in two into the photo multiplier (PM). The same PM received the Doppler signals which were processed by a spectrum analyzer. A computer with a special software, directed the operations. The signal was controlled by an oscilloscope and a recorder.

The laser source is a Spectra Physics Model 2016 Argon Ion laser (maximum power 5 W). A wavelength of 514.5 nm (green) was used, which reduced the maximum power to 2 W. The power used during our experiments varied between 200 and 500 mW.

The photo-multiplier probe (diameter 60 mm) gave a focal length of 160 mm with a beam separation of 38 mm, the angle θ being 0.236 rad. The three axes of the ellipsoid formed by the measuring volume were : $2a = 640\ \mu m$, $2b = 2c = 75\ \mu m$.

The PM was able to move in three directions with the help of three step motors. The calibration factor C, resulting from eq. 5.10, is in our case :

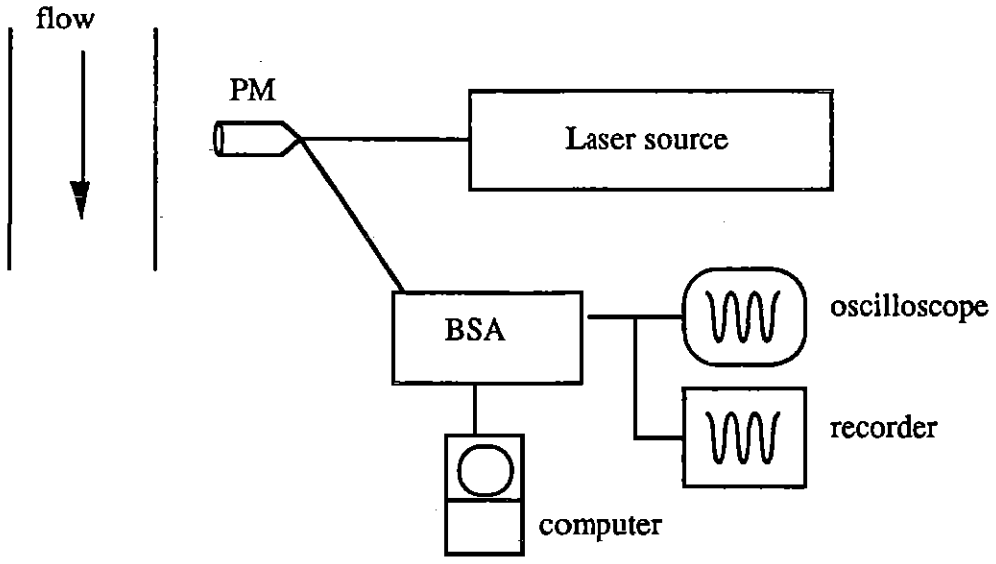

Figure 5.6.

$$C = \frac{V}{f_D} = \frac{\frac{\lambda}{2}}{\sin\frac{\theta}{2}} = 2.182\,\frac{\frac{m}{s}}{MHz} \qquad (5.18)$$

This calibration factor corresponds to the interfringe distance Δy :

$$\Delta y = 2.182\ \mu m \qquad (5.19)$$

Thus, the number of fringes in the intersection region is :

$$N_f = \frac{2b}{\Delta y} = 34 \qquad (5.20)$$

5.3.1. The signal processing.

The processing of the signal was done by the method of the frequency or spectrum analysis. This analysis derives the Doppler spectrum or the probability density function of the Doppler frequency.

The range of Doppler frequencies is scanned by mixing the Doppler signal with a signal of an oscillation frequency f_s. The mixed signal is then viewed by a filter of center frequency f_c and bandwidth BW. The signal that passes through the filter is thus :

$$f_c + \frac{(BW)}{2} \geq f_s \pm f_D \geq f_c - \frac{(BW)}{2} \qquad (5.21)$$

A number of N samples collected of the electric signal constitutes a digitized burst. N is called the record length. The oscillation frequency f_s is also called the sampling frequency. In our case the sampling frequency with which the spectrum analyzer (BSA) operates is :

$$f_s = 1.5 \cdot (BW) \qquad (5.22)$$

The time interval during which a burst is collected is called the record interval R_i:

$$R_i = \frac{N}{f_s} \qquad (5.23)$$

The number of fringes observed by the photo multiplier is then :

$$N_{f,obs} = f_{up} R_i \qquad (5.24)$$

where :

$$f_{up} = f_c + \frac{BW}{2} \qquad (5.25)$$

For velocity values confined between relatively narrow limits and having always the same sign with respect to the bisection of the two beams, the shifting of the frequency with the Bragg cell, explained in the previous section, is not necessary. In this case, the lowest possible absolute value of the velocity to be measured with our equipment is 0.265 mm/s (corresponding to 121.5 Hz). Measurements in the secondary flow-region were carried out using the frequency shift facility (40MHz) since both positive and negative values are encountered in this region.

The center frequency used was zero, and the bandwidth frequency was chosen for each profile in a way such that to have the best signal quality. The bandwidth varied between 7.8 kHz and 250 kHz, though most of the measurements were taken with BW = 31.25 kHz. The sampling frequency is then : $f_s = 46.875$ kHz, and as the record length was chosen N = 64 the record interval was $R_i = 1.365$ ms. The number of fringes observed by the photo multiplier has thus been 21. This avoided undesirable contribution of the outer fringes, where the visibility is bad.

The signal gain which determines the amplification of the input signal was adjusted together with the bandwidth and took values between 20 an 40 dB. The high voltage to the PM varied in general between 1000 and 1800 V.

The particles that pass through the measuring volume should have dimensions comparable to the interfringe, in order to avoid the influence of the particle position to the signal. We have used iriodine particles of a diameter of 2 - 3 μm, which is convenient for our interfringe distance ($\Delta y = 2.18\mu m$).

The Doppler signal was controlled by a Schlumberger type 5013 oscilloscope. The precision of the equipment has been checked by recording series of the bandpass filtered Doppler signal $\left(\frac{f_s}{2} - f_c + f_D\right)$, corresponding to low, well-known velocities. These velocities corresponded to the centerline velocity of water flow through a long tube of a diameter of 9 mm. The signal was recorded in a Sefram type 8211 recorder. With a bandwidth BW=1.95 kHz which gives (eq. 5.22) a sampling frequency of $f_S = 2.925$ kHz and with a flow velocity of 0.2 mm/s, corresponding to $f_D = 0.091$ kHz, the frequency of the signal $\left(\frac{f_s}{2} - f_c + f_D\right)$ varied with time within 0.01 kHz which gives a precision of 0.022 mm/s.

The operations were guided with a Hewlett Packard Vectra QS/16S computer, with the help of an appropriate software.

Particle concentration was high enough so, for each measurement point a number of bursts as high as 1000 was taken in, generally, less than 60 seconds.

5.4. The measurement technique.

When the laser beams pass from the air in another medium, they are refracted. This does not influence the calibration factor, i.e. the proportionality factor between the measured velocity and the Doppler frequency (eq. 5.18). Considering the measuring volume in a medium of refraction index n, the interfringe will be:

$$\Delta y = \frac{\lambda}{2 \sin\frac{\theta}{2}} = \frac{\frac{\lambda_0}{n}}{\frac{2}{n}\sin\frac{\theta_0}{2}} = \frac{\lambda_0}{2 \sin\frac{\theta_0}{2}} = \Delta y_0 \qquad (5.26)$$

and thus it will have the same value as that in the air. The calibration factor being proportional to the interfringe, no further correction is needed. But what has to be considered is the fact that the measuring volume is not displaced in the flow region by the same distance that the PM is displaced in the air :

The beams are refracted twice as they pass from the air to the plexiglass tube and consequently to the solution (Fig. 5.7). Let us assume the PM to be horizontal, the position "1", where the center of the measuring volume is on the separation surface of the Plexiglas tube from the flow region, and the position "2", where the measuring volume is situated at a distance d" from this separation surface. The corresponding distance by which the PM was displaced is d', and the point where each beam intersects with the air-Plexiglas intersection surface has moved by d. It is :

$$n_a \sin\theta_a = n_p \sin\theta_p = n_s \sin\theta_s \qquad (5.27)$$

In our case $\theta_a = 0.236$ rad $/ 2 = 0.118$ rad , and from eq. (5.27) we find : $\theta_s = 0.0812$ rad.

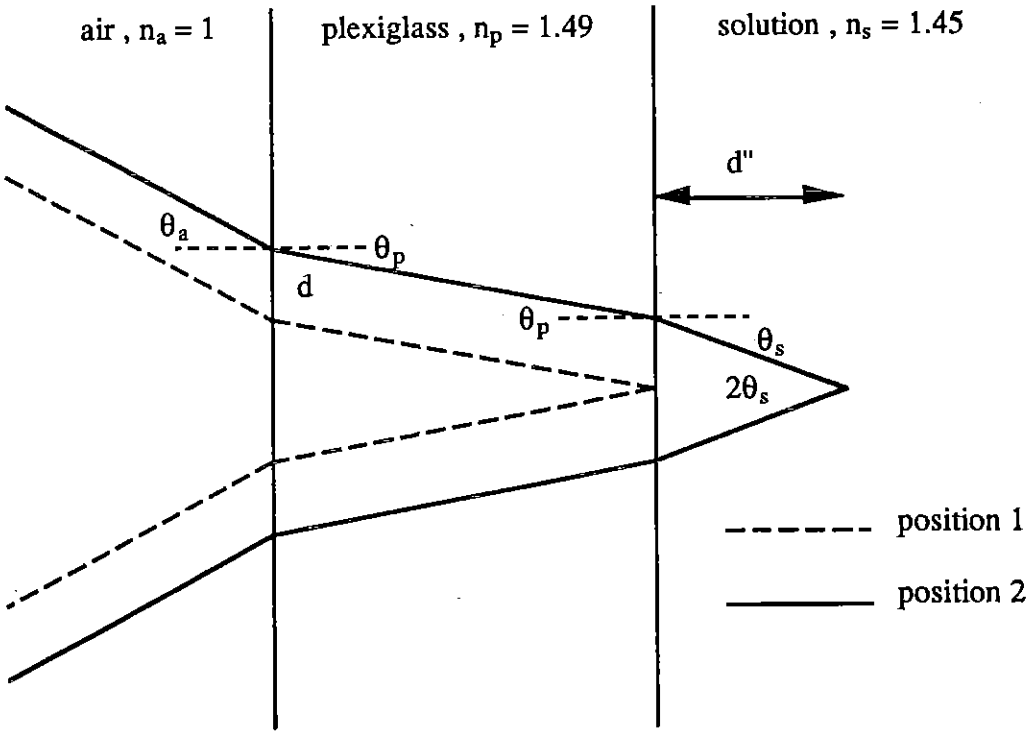

Figure 5.7.

It is easily shown for the displacements d" and d' that:

$$\frac{d''}{d'} = \frac{\frac{d}{\tan\theta_s}}{\frac{d}{\tan\theta_a}} = \frac{\tan\theta_a}{\tan\theta_s} \qquad (5.28)$$

which in our case is : d"/d' = 1.457. Since the angles θ_a and θ_s are very small, one could arrive at approximately the same result by :

$$\frac{d''}{d'} = \frac{\tan\theta_a}{\tan\theta_s} \cong \frac{\sin\theta_a}{\sin\theta_s} = n_s = 1.45 \qquad (5.29)$$

Our measurements covered the vortex region upstream an orifice (Fig. 5.8). For distances higher than 3 mm from the orifice plane ($z < -3$), measurements could be taken by keeping the PM horizontal. The component parallel to the flow direction (U_z) was thus directly measured. The angle α that the flow line formed with the r-direction has been measured for each measurement point, in a picture of the flow about 40 times the real dimensions. The component U_r was then obtained by :

$$U_r = \frac{U_z}{\tan\alpha} \qquad (5.30)$$

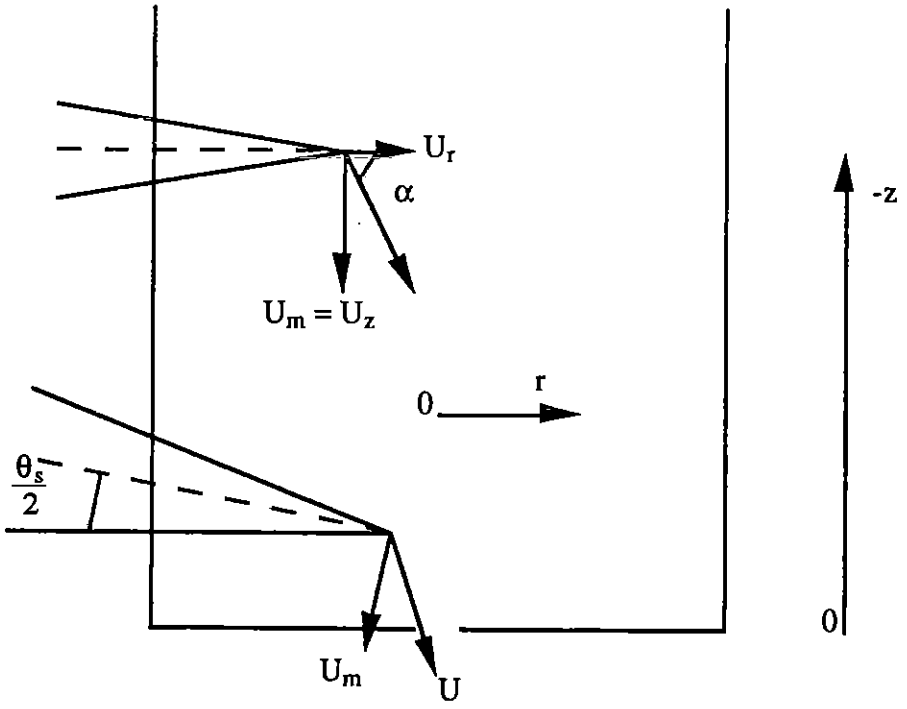

Figure 5.8.

For measurements near the orifice plane, the PM was inclined by an angle of $\theta_s / 2$. In this case, the value of the velocity was first calculated :

$$U = \frac{U_m}{\sin\left(\alpha - \frac{\theta_s}{2}\right)} \qquad (5.31)$$

and the two components were then derived :

$$U_z = U \sin \alpha \quad \text{and} \quad U_r = U \cos \alpha \qquad (5.32)$$

5.5. Results

The fluid

The velocity field of a polymer solution is examined in this section. It is a 100 ppm polyacrylamide solution in a glucose/water syrup (80%/20% respectively in weight). The polymer is a sample of partially hydrolysed polyacrylamide (HPAM) commonly used in oil recovery (Dow P700). Its molecular weight was found $4.1 \cdot 10^6$ $g \cdot mol^{-1}$ by the GPC method (annex D).

The solution was prepared by mixing together polymer-water and glucose-water mixtures of the necessary composition in order to obtain the desired final composition. The fluid contained also NaCl (20g/lt), in order to obtain a coiled rest state configuration.

The orifice flow

The shear viscosity of this solution is almost independent on shear rate (1.5 Pas). Its flow curve through the orifice of Φ= 1.22 mm was extensively studied in [17]. Flow conditions corresponding to the beginning of the intermediate regime (vortex growth) were chosen (q_v= 74.0 mm^3/s, U= 63.3 mm/s). The flow pattern is shown in Fig. 5.21. The vortices have been asymmetric due to a slight asymmetry in the flow geometry. As mentioned in section 1, Xu et al. reported also significant asymmetries in the flow pattern due to slight asymmetries in the geometry.

Measurements were first taken with the solvent, that is, with the mixture of glucose and water before we passed to the solution.

5.5.1. Measurements on the solvent

The theoretical solution of the Stokes problem for the creeping flow of an incompressible Newtonian fluid through a circular hole in an infinite plane wall [18], is based on the Stokes stream function :

$$\psi = \frac{Q}{2\pi}(1 - \cos\eta) \qquad (5.33)$$

where η is one member of the oblate spheroidal coordinate system (ξ , η) defined as :

$$r = \frac{1}{2}\Phi \cosh\xi \sin\eta \qquad z = \frac{1}{2}\Phi \sinh\xi \cos\eta \qquad (5.34)$$

The coordinate surfaces of constant η and, hence, the stream surfaces of constant ψ, are confocal hyperboloids of revolution. The surfaces of constant ξ are oblique spheroids. The cut-off of the surfaces of constant ψ in a central plane are shown schematically in Fig. 5.9 :

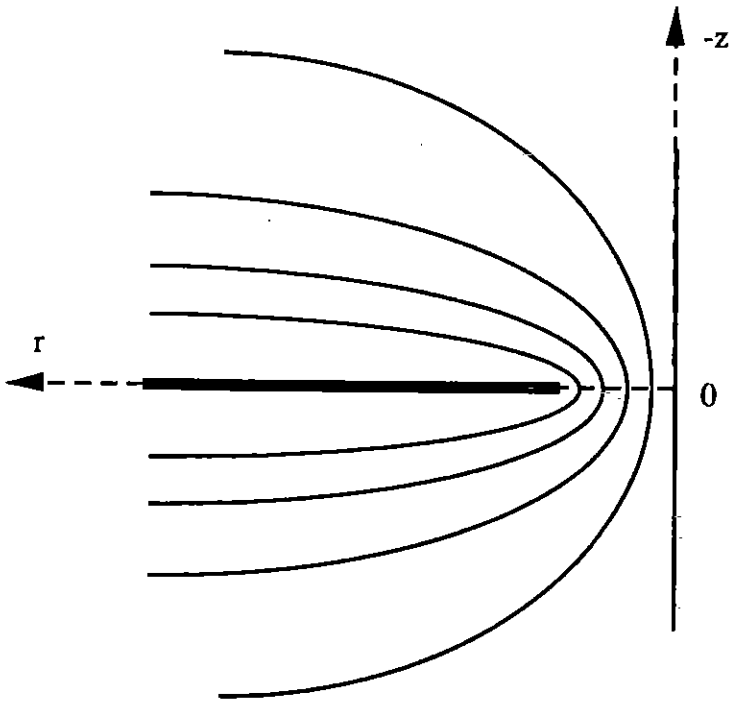

Figure 5.9.

These hyperbolas represent the flow lines. The velocity profile on the centerline is then given by :

$$U_z(z) = \frac{6\,q_v}{\pi\,\Phi^2}\,\frac{1}{1+\left(\frac{2z}{\Phi}\right)^2} \quad \text{or} \quad \frac{U_z(z)}{U} = \frac{3}{2+8\left(\frac{z}{\Phi}\right)^2} \qquad (5.35)$$

where U is the average velocity at the orifice. This theoretical profile can be used as an approximation for contraction flows of Newtonian liquids in the case of a high contraction ratio and close to the contraction level.

The contraction ratio in our case is 20 mm / 1.22 mm = 16.4. The centerline profile of our solvent is shown in Fig. 5.10. The flow rate was very close to the one chosen for the solution. At a point as close as possible to the contraction plane the velocity has the expected value of 1.5 times the average value. It matches perfectly with eq. 5.35 for $z/\Phi < 0.7$. For distances of the orifice higher than that, the equation deviates as it tends towards a zero velocity. At about $z/\Phi = 20$, U_z has the upstream developed value of twice the average velocity in the upstream tube.

5.5.2. Measurements with the solution.

5.5.2.1. The developed profile upstream.

The profile of U_z along the r-direction was measured at a section far upstream the orifice plane (z= -50 mm, $2z/\Phi$= -83.3), one of the two sections between which the differential pressure was measured. The profile, non-dimensionalized with the average velocity in the upstream tube U_u, is compared in Fig. 5.11 with the Poiseuille velocity distribution :

$$\frac{U_z}{U_u} = 2\left(1 - \left(\frac{r}{R_u}\right)^2\right) \qquad (5.36)$$

where R_u is the upstream tube radius. As $n \cong 1$ for this fluid, its developed profile should not differ from that of a Newtonian fluid. This result shows that the velocity profile at this section is not disturbed by the existence of the orifice.

5.5.2.2. The axial profile.

The evolution of U_z on the flow axis was also measured. It is compared in dimensionless form with that of the solvent in Fig. 5.12. As expected, the presence of the vortices results in much higher velocities near the contraction plane. On the other hand, the velocity is undisturbed closer upstream than in the case of the solvent : Until about 13 diameters upstream: $U_z = 2 \cdot U_u$.

In the region between $-10\Phi < z < -5\Phi$ the slope of the log-log plot of the velocity is about 3, which leads to the conclusion that :

$$U_z \approx (-z)^{-3} \quad \text{and} \quad \dot{\varepsilon} = \frac{dU_z}{dz} \approx (-z)^{-4} \qquad (5.37a)$$

that is, the stretch rate on the centerline varies as z^{-4}.

In the region $-2\Phi < z < -0.5\Phi$, which is the minimum distance from the orifice attained, a slope of about 1/4 was found, indicating that near the orifice the stretch rate varies as $z^{-(5/4)}$:

$$\dot{\varepsilon} \approx (-z)^{-(5/4)} \qquad (5.37b)$$

The profile is shown in lin-log form in Fig. 5.13. This representation shows that an exponential law fits the velocity variation for $z/\Phi > 6$. At $z = -2.2\Phi$ there is a sudden slope change in the curve which in the picture of the flow seems to correspond to the point where flow lines become almost parallel to the vertical axis. From the Fig. 5.13 the following empirical laws are obtained :

$$6 > \frac{-z}{\Phi} > 2 \quad \rightarrow \quad \frac{U_z}{U} = 2.07\, e^{-0.59 \frac{z}{\Phi}} \qquad (5.38a)$$

$$2 \geq \frac{-z}{\Phi} > 0 \quad \rightarrow \quad \frac{U_z}{U} = 1.05\, e^{-0.24 \frac{z}{\Phi}} \qquad (5.38b)$$

An estimation of the evolution of the stretch rate with z can be obtained by plotting $\frac{\Delta U_z}{\Delta z}$ (Fig. 5.14). The high dispersity of the calculated stretch rate is due to the following fact: If one uses very small distances between neighboring points of the velocity measurements, the uncertainty of the interval is added to the one of the two velocity values. In the opposite case (high distance intervals), the evolution of the stretch rate is lost. The maximum stretch rate can also be calculated by direct derivation of relations (5.38) :

$$6 > \frac{-z}{\Phi} > 2 \quad \rightarrow \quad \dot{\varepsilon} = 63.3\, e^{-0.51 \frac{z}{\Phi}}\ s^{-1}$$

$$2 \geq \frac{-z}{\Phi} > 0 \quad \rightarrow \quad \dot{\varepsilon} = 13.3\, e^{-0.24 \frac{z}{\Phi}}\ s^{-1}$$

The corresponding curves are shown in Fig. 5.14. In the upper part of the converging zone $\dot{\varepsilon}$ increases from values close to zero at $z/\Phi = 10$ up to a value of 23 s^{-1} at the distance from the orifice where streamlines become almost parallel with the vertical. The subsequent break in the $U_z(z)$ curve corresponds to a sudden decrease of $\dot{\varepsilon}$ and subsequent much slower increase.

Profiles similar to the one of Fig. 5.13 are presented for polyacrylamide (Separan) solutions of the same concentration range by Hasegawa and Iwaida [11]. The distance of the breakpoint in the $U_z(z)$ curve from the orifice plane increases with flow rate.

In order to study the development of the axial velocity profile, we normalized it with respect to the region included between the vortices. The dimensionless procedure involved division of the velocity with the average velocity in the vortex region defined by :

$$U_v = \frac{R_d^2}{R_v^2} U \qquad (5.39)$$

where R_v is the radius of the main flow region (Fig. 5.15). As the flow in our case was asymmetric, the average value between both sides:

$$R_{v,avg} = \frac{R_{v,left} + R_{v,right}}{2} \qquad (5.40)$$

was taken into account in the Fig. 5.15. Further on (Fig. 5.18, 5.19 and 5.22), R_v is considered separately for each case (left and right).

Cable and Boger [7] presented the normalized axial profile of a shear-thinning aqueous Separan solution of n= 0.37 in the vortex growth regime in a 4:1 contraction. It increases from its developed value far upstream of (3n+1)/(n+1) to a maximum that occurs at a point very close to the vortex detachment plane, then it decreases monotonically until the same fully-developed downstream value. It obtains this value at a fraction of Φ upstream the contraction plane.

In our case the normalized U_z (Fig. 5.15) increases in the same way until the vortex detachment plane. It then decreases to a minimum of 2/3 at Φ= -3.5, and then increases again towards its developed value which has not been attained. It seems that in our thin-walled submerged-jet configuration the profile at the orifice level is quite homogeneous.

5.5.2.3. The profiles at upstream sections

The velocity was also measured at the same regime along upstream sections. As previously noted, the vortex torus has been asymmetric. But the flow pattern remained constant with time as it was shown by repeated pictures of the flow. Measurements were taken at sections in the region -2 mm $\geq z \geq$ -10 mm. The positions of these sections in the flow pattern are shown schematically in Figure 5.16a. The radius of the main flow region as a function of the distance from the orifice is shown in Fig. 5.16b.

The components U_Z and U_r have been derived by using the procedure described in section 5.4. The profiles of the U_Z component are shown in Figure 5.17. We should remark here the consequences of the asymmetry : at the section z= -10 mm for example, the left side (represented with negative r values), is in the vortex region resulting in negative velocities, while the right side (positive r), contains only positive values.

In order to substantiate our data, an integration of the U_z component was performed according to :

$$Q = \int_0^r 2\pi r U_z \, dr \qquad (5.41)$$

The values of Q deduced for each measurement section agreed with the measured flow rate within +/-9.5 %. This agreement is considered quite satisfactory, taking into account the fact that the relatively small velocity values in the vortex region are integrated over large surfaces.

In Figure 5.18 the axial distance is non-dimensionalized by the radius of the main flow region R_v for each section. The asymmetry was taken into account by taking different R_v values at each side. An important remark to be made here is that at $r/R_v = 1$ the U_z values are far from being negligible, in contradiction with the suppositions of Cogswell and Binding in their attempts to estimate the extensional viscosity from contraction flow data. The ratio $U_z(1)/U_z(0)$ obtains values of more than 0.5 in some cases, especially at the sections z= -6 mm and z= -4 mm which are halfway between the vortex detachment plane and the contraction plane.

The normalized profiles of U_z are presented in Figure 5.19. The average velocity defined by eq. 5.39 is used for this purpose. As previously mentioned, the same normalization procedure has been used by Cable and Boger. They showed that the U_z component profile, overdeveloped in the vortex detachment plane, and relaxed back to become fully developed again near the contraction plane. In the present experiments the contraction ratio is much higher. The profile is indeed overdeveloped at z= -10 mm which corresponds approximately to the vortex detachment plane and $U_z(0)/U_v = 48$. It relaxes back as one approaches the contraction plane but it is far from being fully developed at z= -2 mm. This fact must be attributed to the much higher contraction ratio.

The U_r component profiles are shown in Figure 5.20. We should remark here that the asymmetry has more pronounced effects, especially in the middle vortex region (z= -4 mm and z= -3 mm). At z= -2 mm, $U_z = 0$ within $|z| < 2 R_d$, as the flow lines followed perfectly the direction of the flow. Negative values of U_r exist for $|z| > 2 R_d$ as the flow lines diverge abruptly to enter into the recirculation region.

The lines of constant U_z and U_r values in the vortex region are shown in Figure 5.21. The values plotted there represent mm/s. Green lines represent U_z and red lines U_r. We notice once more that the velocity values in the inner side of the vortices are of the same order of magnitude as those in the main flow region.

We have previously mentioned that the theories of Cogswell and Binding concerning the derivation of the extensional viscosity from contraction flow data are

based on the assumption that at each section of the main flow region the flow is fully developed. This would mean that we should obtain a master curve by plotting :

$$\frac{U_z(r)}{U_z(0)}\left(\frac{r}{R_v}\right) \qquad (5.42)$$

for any z. This proved not to be the case in our measurements. We noticed though that there seemed to be a shift in these curves which increased as one moved away from the vortex detachment plane. We then considered the height of the vortices X (different for each side), and plotted :

$$\frac{U_z(r)}{U_z(0)}\left(\frac{r}{R_v}\frac{z}{L_v}\right) \qquad (5.43)$$

where L_v is the vortex reattachment length.
The measurements at the different sections of the upper half of the vortices (-4 mm $\geq$ z $\geq$ -10 mm) matched together (Fig. 5.22). The asymmetry is again obvious in this master curve.

The master curve of Fig. 5.22 shows that, in order to consider a velocity profile in the upper region of the vortex, that is, in the region where the major velocity rearrangements take place, one has to consider a radius equal to :

$$R = \frac{3}{2}\frac{R(z)}{z}L_v \qquad (5.44)$$

rather than simply consider R(z). This is, of course, not valid for the lower region of the vortex where the velocity profile is already almost rearranged (Fig. 5.23). As one approaches the orifice, the velocity profile moves away from the master curve.

5.6. Conclusions.

In the present chapter, we have been interested in the velocity field upstream of an orifice flow of a flexible polymer solution. The flow of that same solution has been previously the object of extensive studies in our Laboratory [i.e. 17]. The flow regime chosen to examine corresponds to the beginning of the vortex growth regime. The contraction ratio (16.7) is very large.

The method of LDV has been used for the velocity measurements. After having established the measurement technique from the optical point of view, measurements on the flow of the Newtonian solvent (a glucose/water mixture of 80/20 w.) showed the

evolution of its axial profile. This profile is in good agreement with the theoretical solution of a flow through a circular hole for half a diameter upstream. At higher distances the theoretical solution predicts lower velocities, since it is valid for an infinite contraction ratio.

Measurements with the solution at an upstream section ($z/\Phi = -42$), showed a developed profile which followed the Poiseuille distribution for the flow of a Newtonian fluid through a tube. This section represented one of the two points where differential pressure measurements have been carried out whenever the submerged jet configuration has been used throughout this work (chapters 2 and 3). Thus, the undisturbed profile existing at this point validated the pressure measurements.

The axial profile has shown that the maximal stretch rate (about 23 s^{-1}) occurs about 2 diameters upstream, in the point where pictures of the flow have shown that the streamlines in the main flow region become almost parallel. This point is characterised by a break in the $U_z(z)$ curve on the axis. This break point corresponds to a sudden decrease of the rate of extension along the axis.

The axial profile normalized with the average velocity in the vortex region proved to differ from that presented by Cable and Boger for the contraction flow through a tube : It presented a local minimum 3.5 diameters upstream.

The normalized transversal profile, overdeveloped at the vortex detachment plane, relaxed back till $z/\Phi = -1.7$. It was though far from being fully relaxed at this distance from the orifice.

Profiles at sections in the vortex region proved that, in the limits of the vortex the velocity can attain values until 60% of the velocity on the axis and cannot, thus, be neglected. A similarity of all profiles of the axial component in the upper half of the vortex torus has been found. This fact indicated that a radius of the main flow region, modified by a parameter which takes into account the relative position in the vortex should be considered in future modelization of the velocity profile.

References

1. M. Collins and W.R. Schowalter, "Behavior of non-newtonian fluids in the entry region of a pipe", AIChEJ, 9 (1963) 804.
2. F.N. Cogswell, "Converging flow and stretching flow : A compilation", J. Non Newt. Fluid Mech., 4 (1978) 23-38.
3. D.M. Binding and K. Walters, "On the use of flow through a contraction in estimating the extensional viscosity of mobile polymer solutions", J. Non Newt. Fluid Mech., 30 (1988) 233-250.
4. M.P. Brocklebank and J.M. Smith, "Laminar velocity profile development in straight pipes of circular cross section", Rheologica Acta, 7 (1968) 286-289.
5. D.V. Boger and A.V. Ramamurthy, "Flow of viscoelastic fluids through an abrupt contraction", Rheologica Acta, 11 (1972) 61-69.
6. A.V. Ramamurthy and D.V. Boger, "Developing velocity profiles on the downstream side of a contraction for inelastic polymer solutions", Trans. Soc. Rheology, 15:4 (1971) 709-730.
7. P.J. Cable and D.V. Boger, "A comprehensive experimental investigation of tubular entry flow of viscoelastic fluids.", AIChJ:
   "Part I: Vortex characteristics in stable flow", 24 (1978) 869;
   "Part II: The velocity field in stable flow", 24 (1978) 992;
   "Part III: Unstable flow", 25 (1979) 152.
8. R.J. Binnington, G.J. Troup and D.V. Boger, "A low-cost laser-speckle photographic technique for velocity measurement in slow flows", J. Non Newt. Fluid Mech., 12 (1983) 255-267.
9. E.T. Busby and W.C. MacSporran, "An experimental study of nonrheometric flows of viscoelastic fluids. I. Flow into a re-entrant tube", J. Non Newt. Fluid Mech., 1 (1976) 71-82.
10. A.V. Ramamurthy and J.C.H. McAdam, "Velocity measurements in the die entry region of a capillary rheometer", Trans. Soc. Rheology, 24 (1980) 167-188.
11. T. Hasegawa and T. Iwaida, "Experiments on elongational flow of dilute polymer solutions", J. Non Newt. Fluid Mech.:
    "Part I: Jet reaction and excess pressure drop for the flow through small apertures", 15 (1984) 257-277.
    "Part II: Velocity field for the flow through small apertures", 15 (1984) 279-307.
12. Y. Xu, P. Wang and R. Qian, "Velocity field of convergent flow into a rectangular slit for a polymeric fluid", Rheologica Acta, 25 (1986) 239-245.
13. A.M. Wunderlich, P.O. Brun and F. Durst, "Flow of dilute polyacrylamide solutions through a sudden plannar contraction", J. Non Newt. Fluid Mech., 28 (1988) 267-285.

14. J.V. Lawler, S.J. Muller, R.A. Brown and R.C. Armstrong, "Laser Doppler velocimetry measurements of velocity fields and transitions in viscoelastic fluids", J. Non Newt. Fluid Mech., 20 (1986) 51-92.
15. G. H. McKinley, W. P. Raiford, R. A. Brown and R.C. Armstrong, "Nonlinear dynamics of viscoelastic flow in axisymmetric abrupt contractions", J. Fluid Mech., 223 (1991) 411-456.
16. W.P. Raiford, L.M. Quinzani, P.J. Coates, R.C. Armstrong and R.A. Brown, "LDV measurements of viscoelastic flow transitions in abrupt axisymmetric contractions: Interaction of inertia and elasticity", J. Non Newt. Fluid Mech., 32 (1989) 39-68.
17. U. Cartalos and J.M. Piau, "Pressure drop scaling laws and structural stress contributions for complex flows of flexible polymer solutions in thick solvents", J. Non Newt. Fluid Mech., 44 (1992) 55-83.
18. J. Happel and H. Brenner, "Low Reynolds Number Hydrodynamics", Prentice Hall ed., Engelwood Cliffs, NJ, 1965.
19. R. Comolet, "Mécanique expérimentale des fluides", Masson ed., 1982.

TABLES AND FIGURES

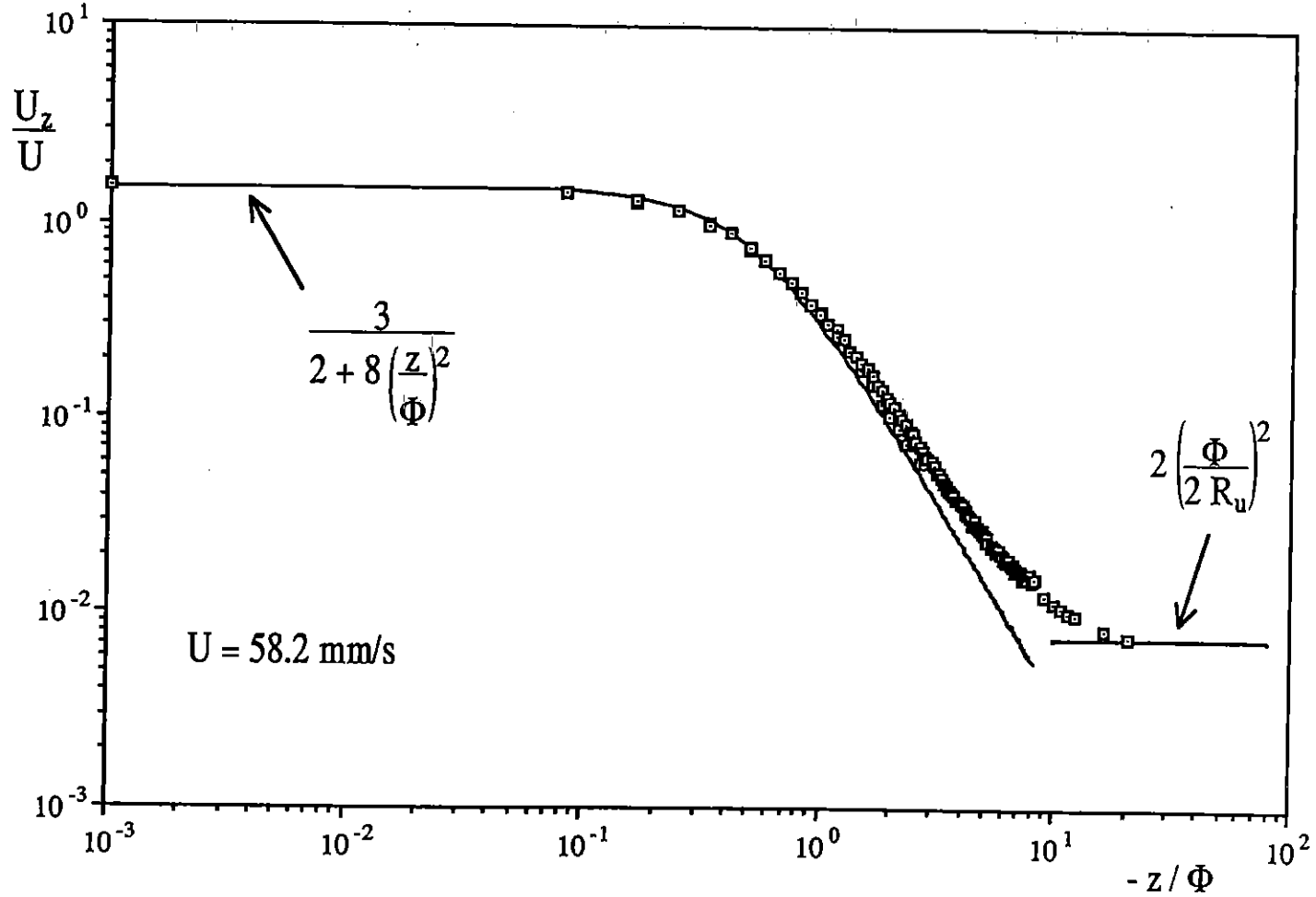

Figure 5.10 : Comparison of measurements on the flow axis with the theoretical profile for the solvent

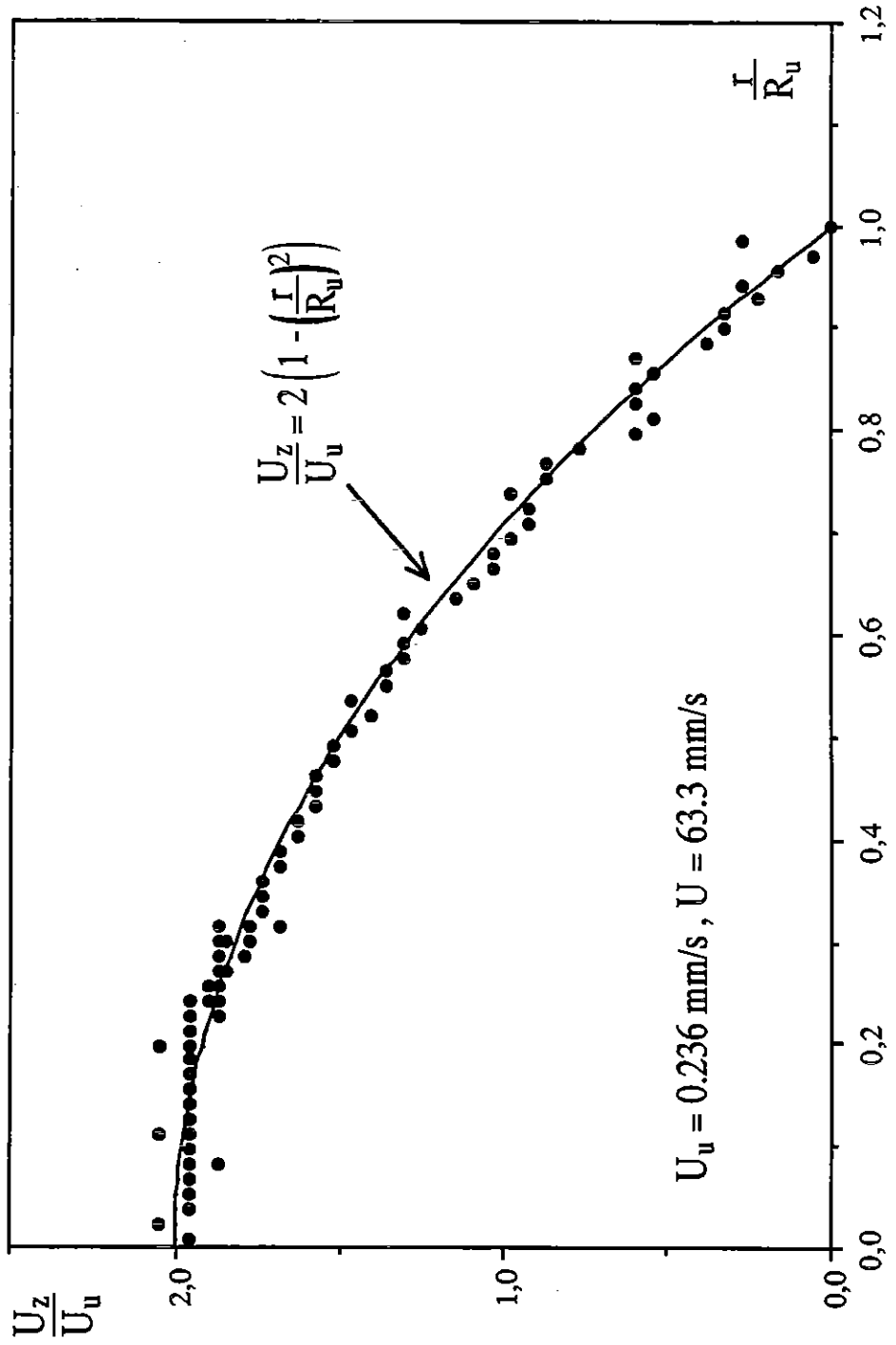

Figure 5.11 : Adimensional profile of Uz(r) at the position z= -50 mm.

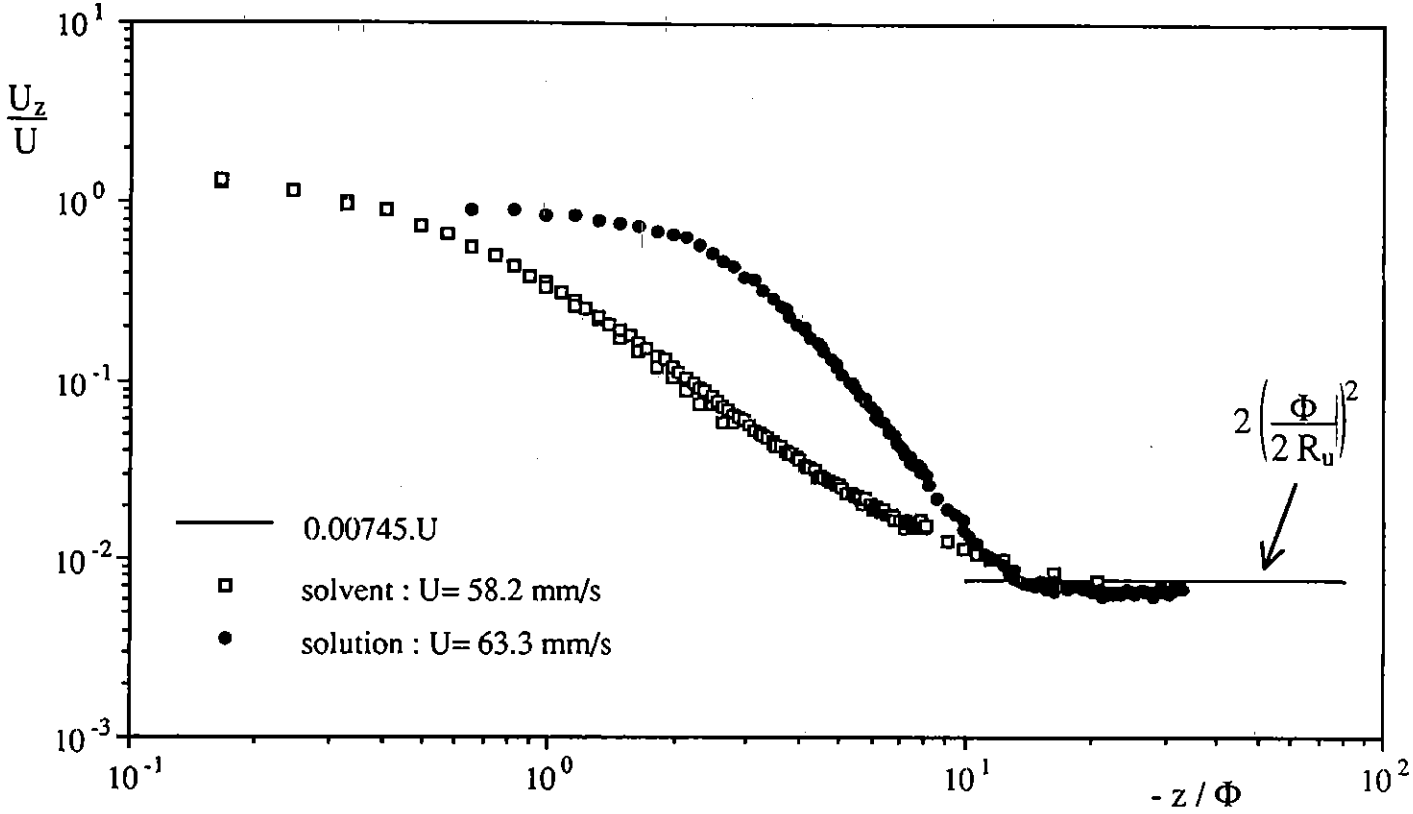

Figure 5.12 : Comparison of the axial profile of the solution with that of the solvent

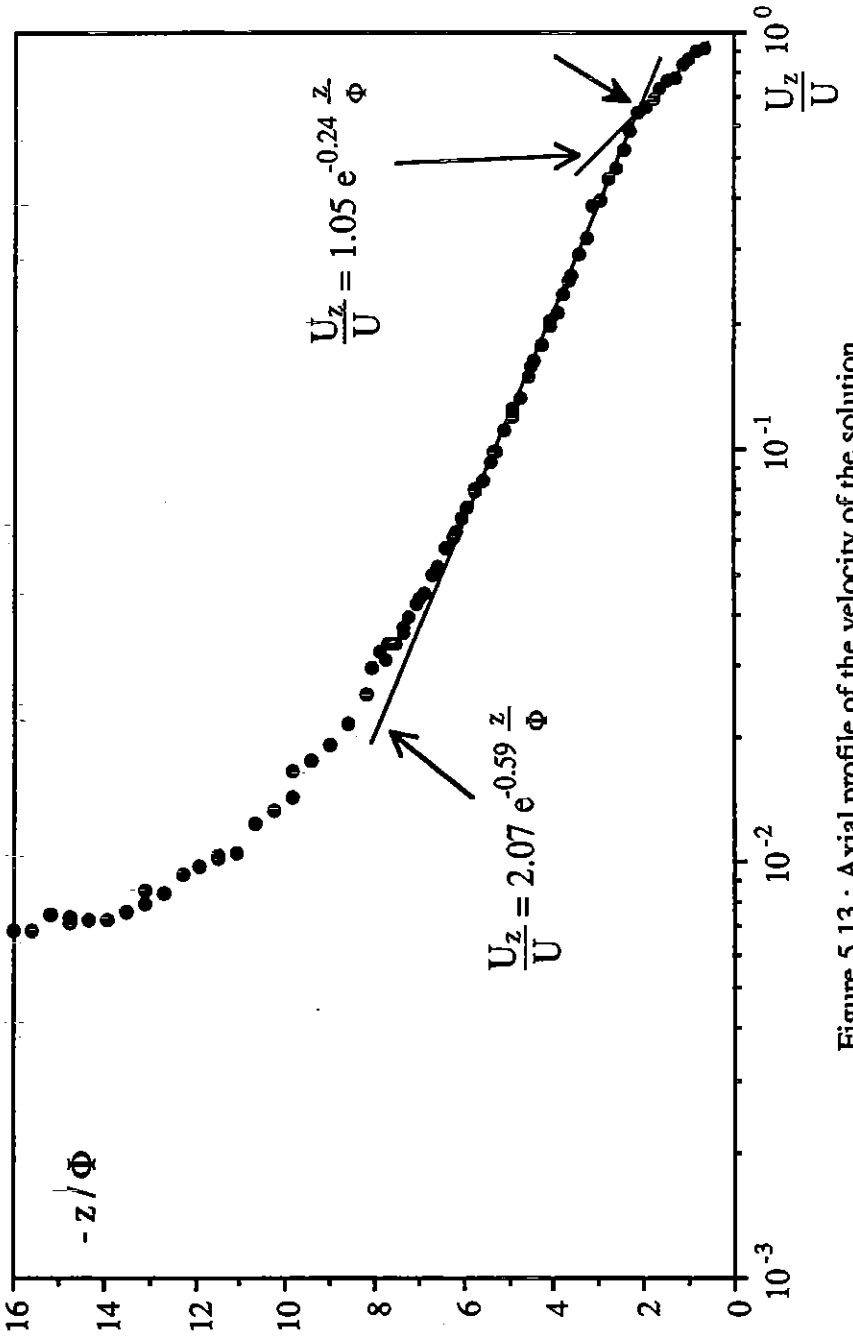

Figure 5.13 : Axial profile of the velocity of the solution.

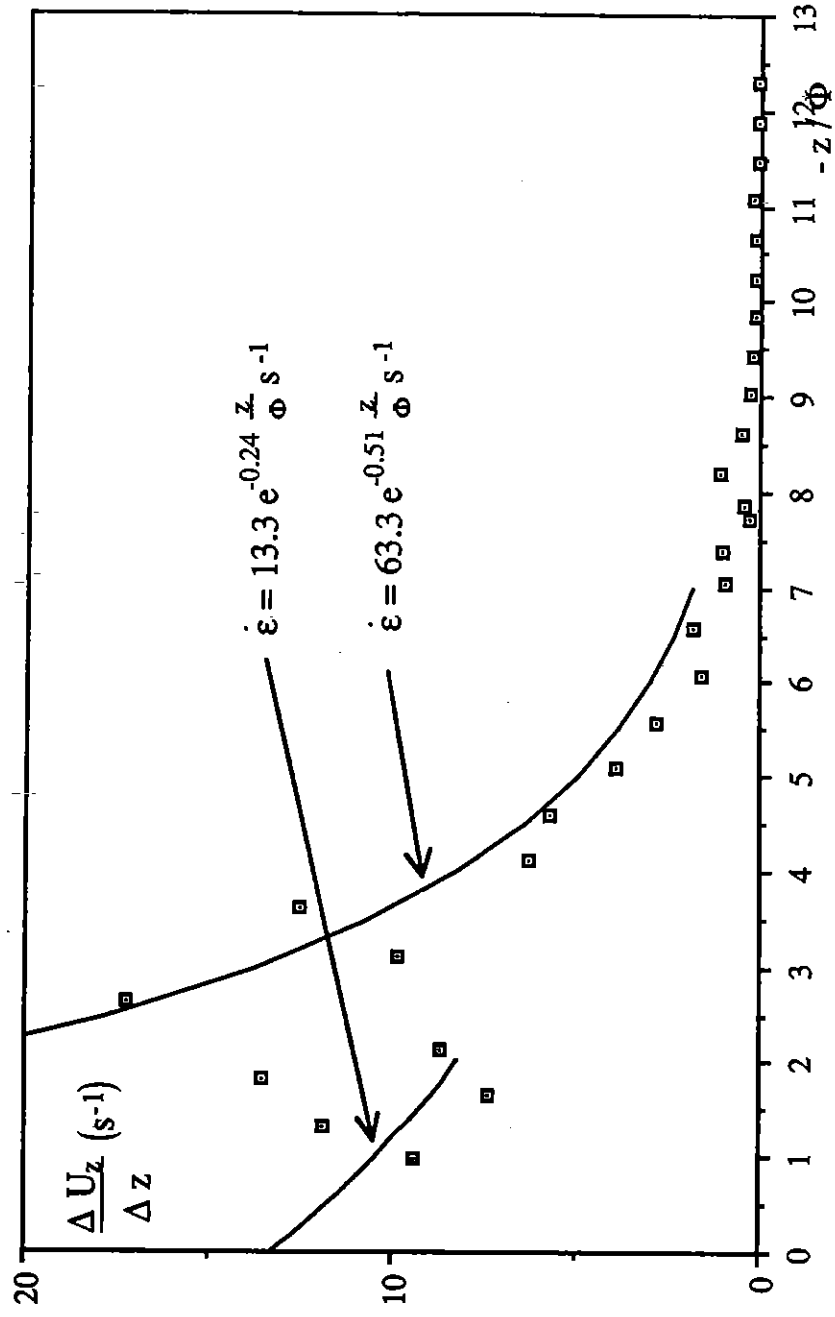

Figure 5.14 : Estimation of the stretch rate on the axis

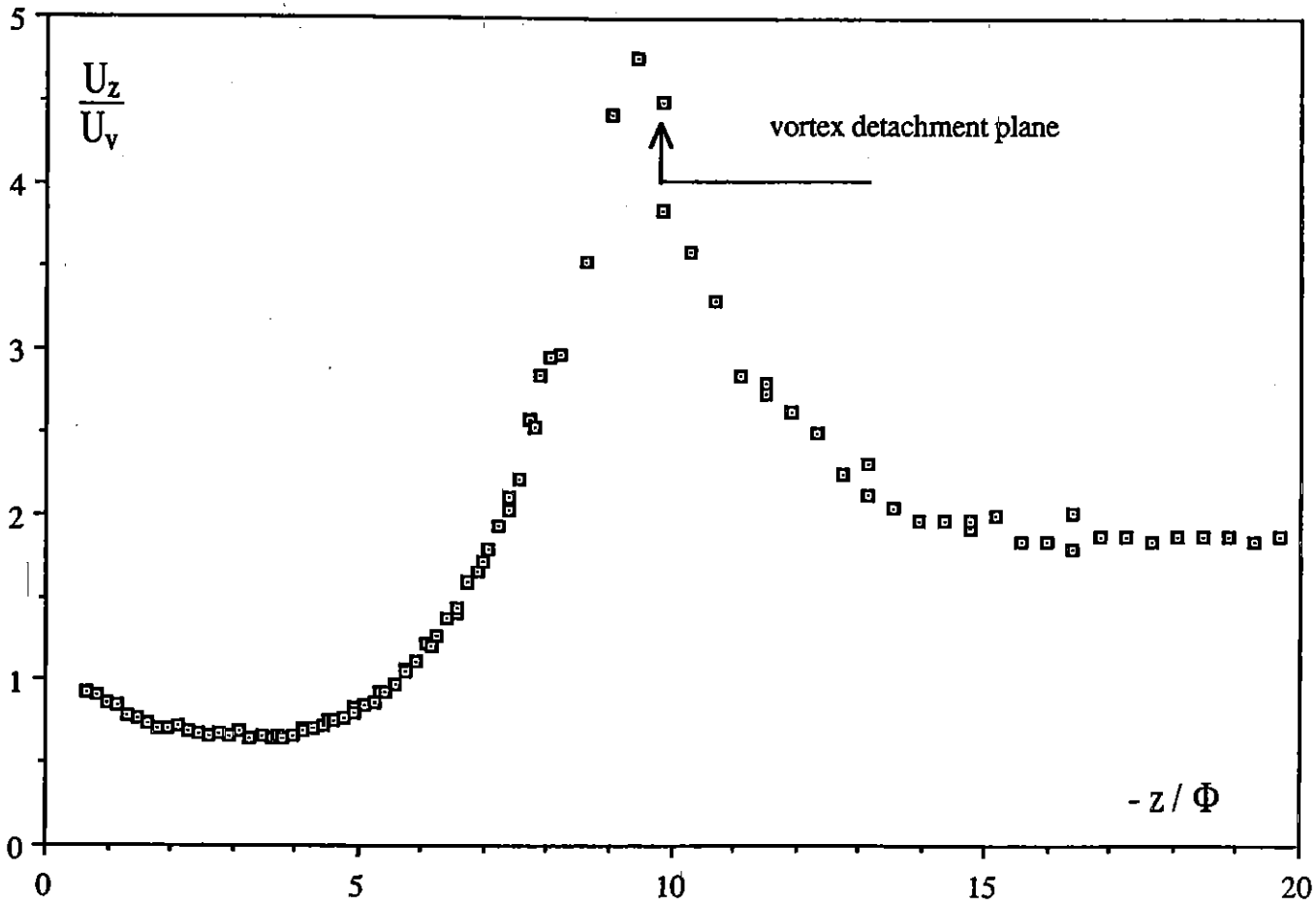

Figure 5.15 : The normalized axial profile.

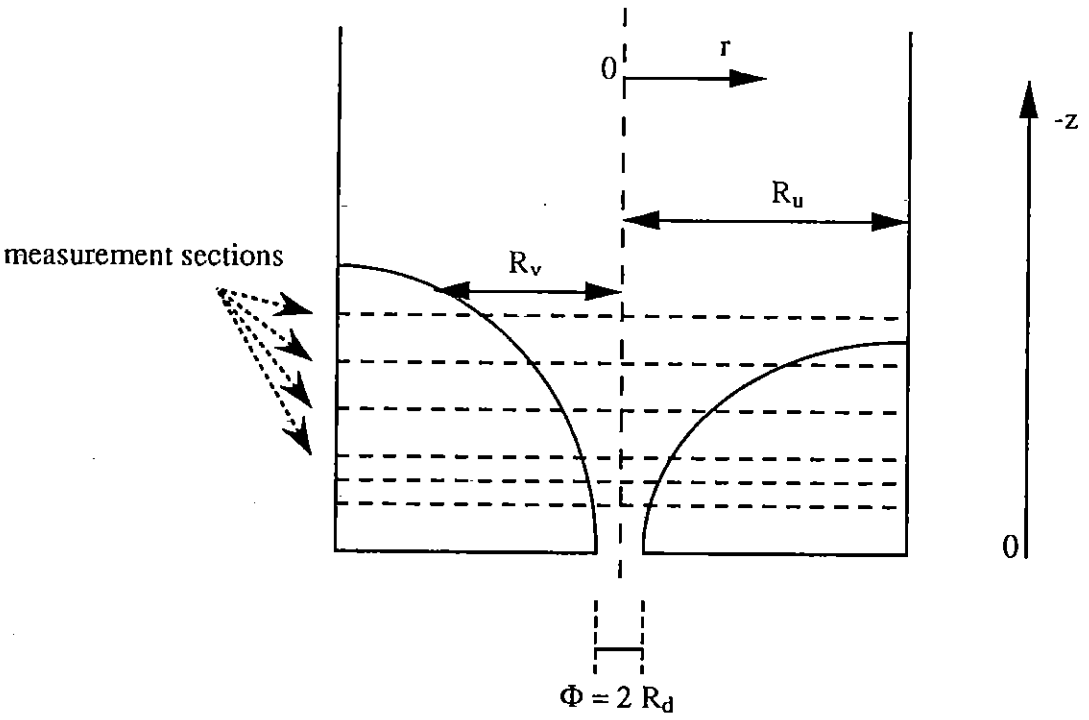

Figure 5.16a : The positions of the measurement sections in the flow pattern.

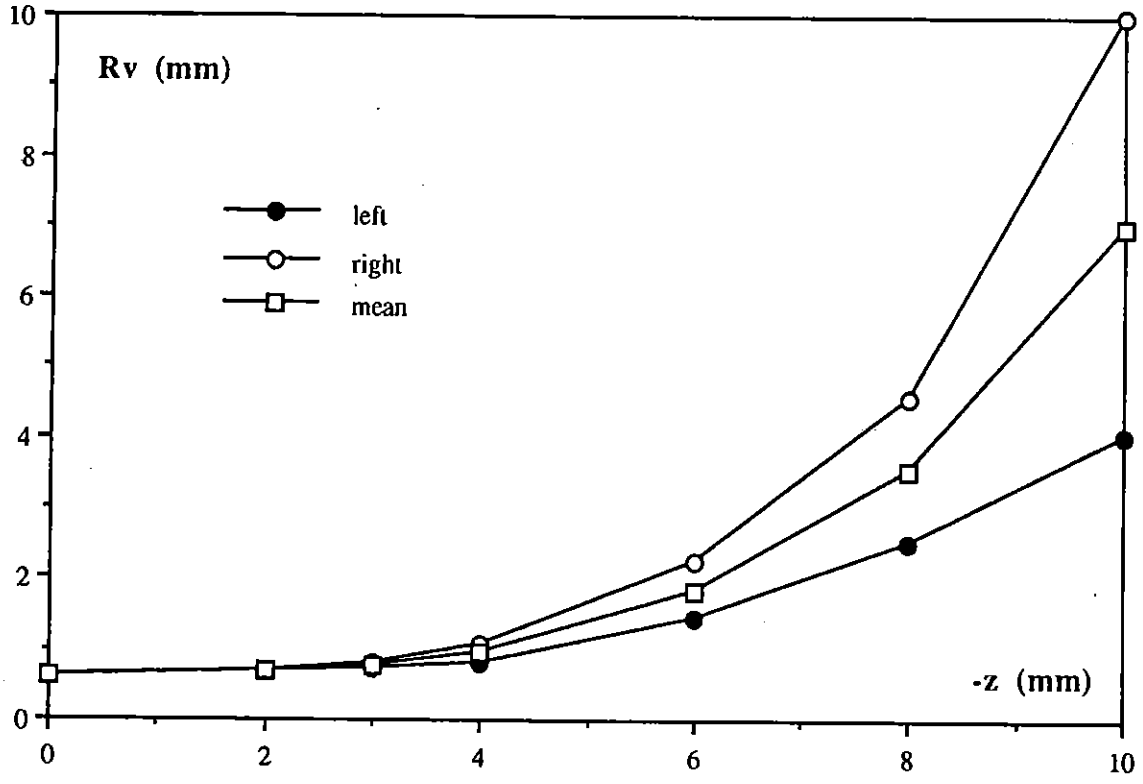

Figure 5.16b : The radius of the main flow region as a function of the distance from the orifice.

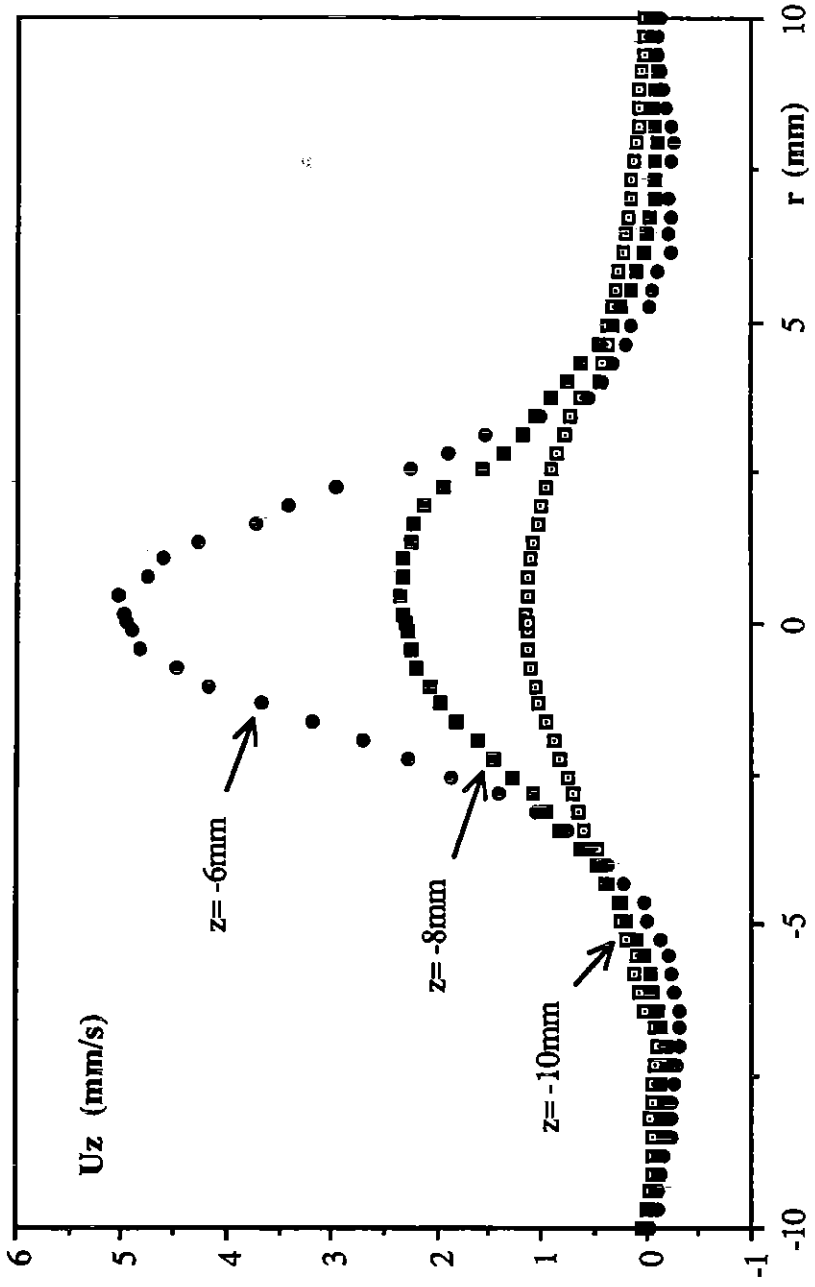

Figure 5.17a : Profiles of the Uz component : profiles at z= -10, z= -8 and z= -6mm

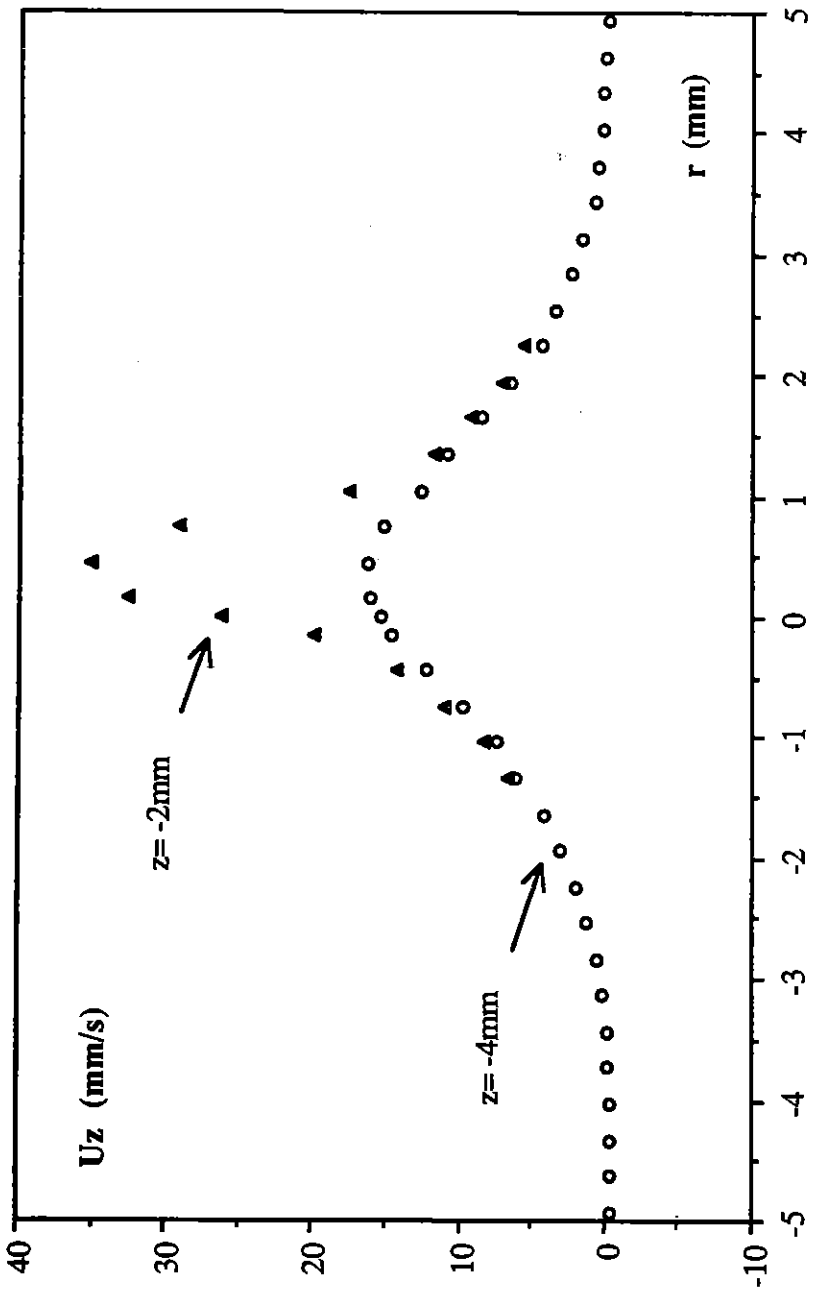

Figure 5.17b : Profiles of the Uz component : profiles at z= -4, and z= -2mm

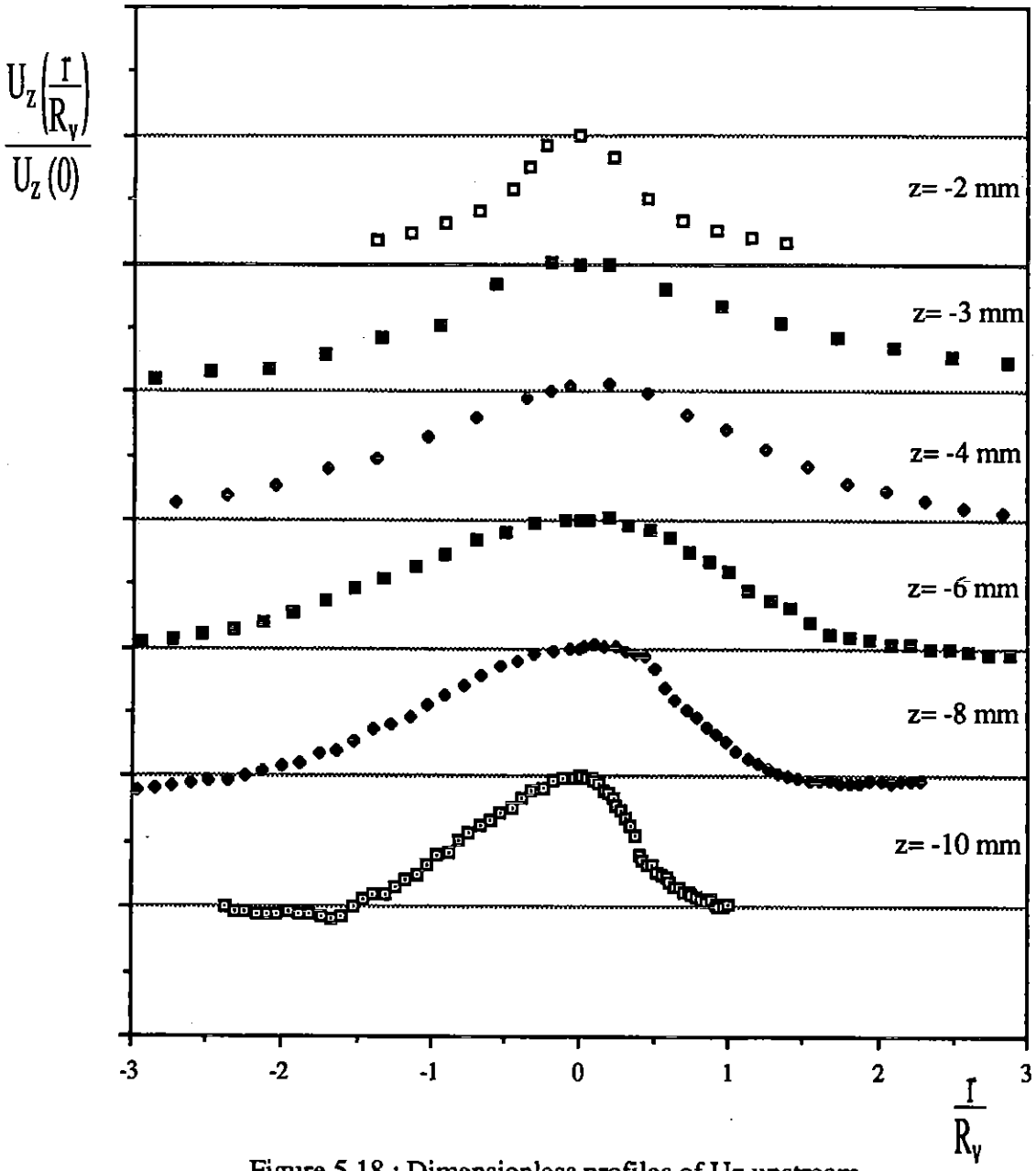

Figure 5.18 : Dimensionless profiles of Uz upstream

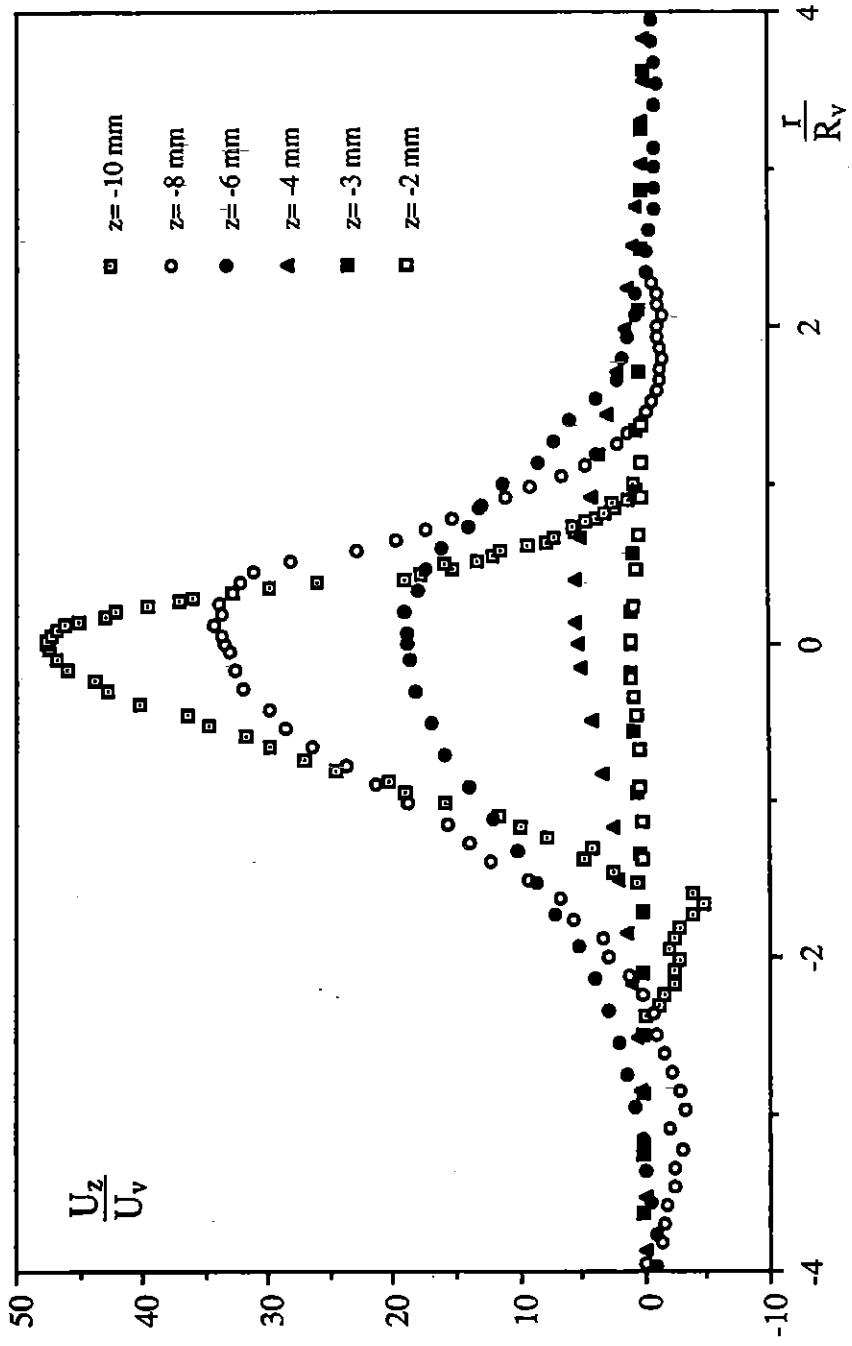

Figure 5.19 : Normalized profiles of Uz

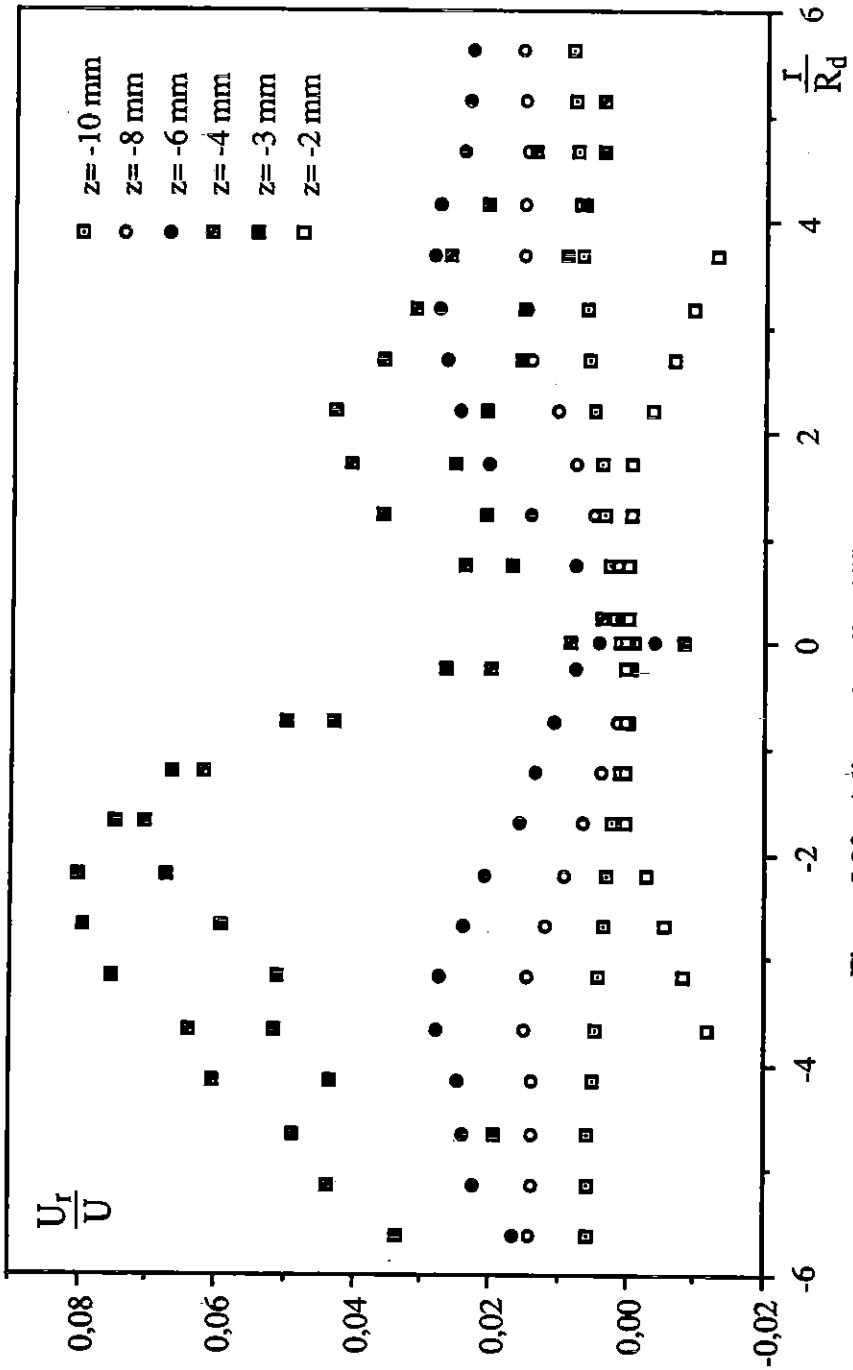

Figure 5.20 : Adimensionalized Ur component profiles

Figure 5.21 : The contour lines of the two velocity components: Uz (green) and Ur (red).

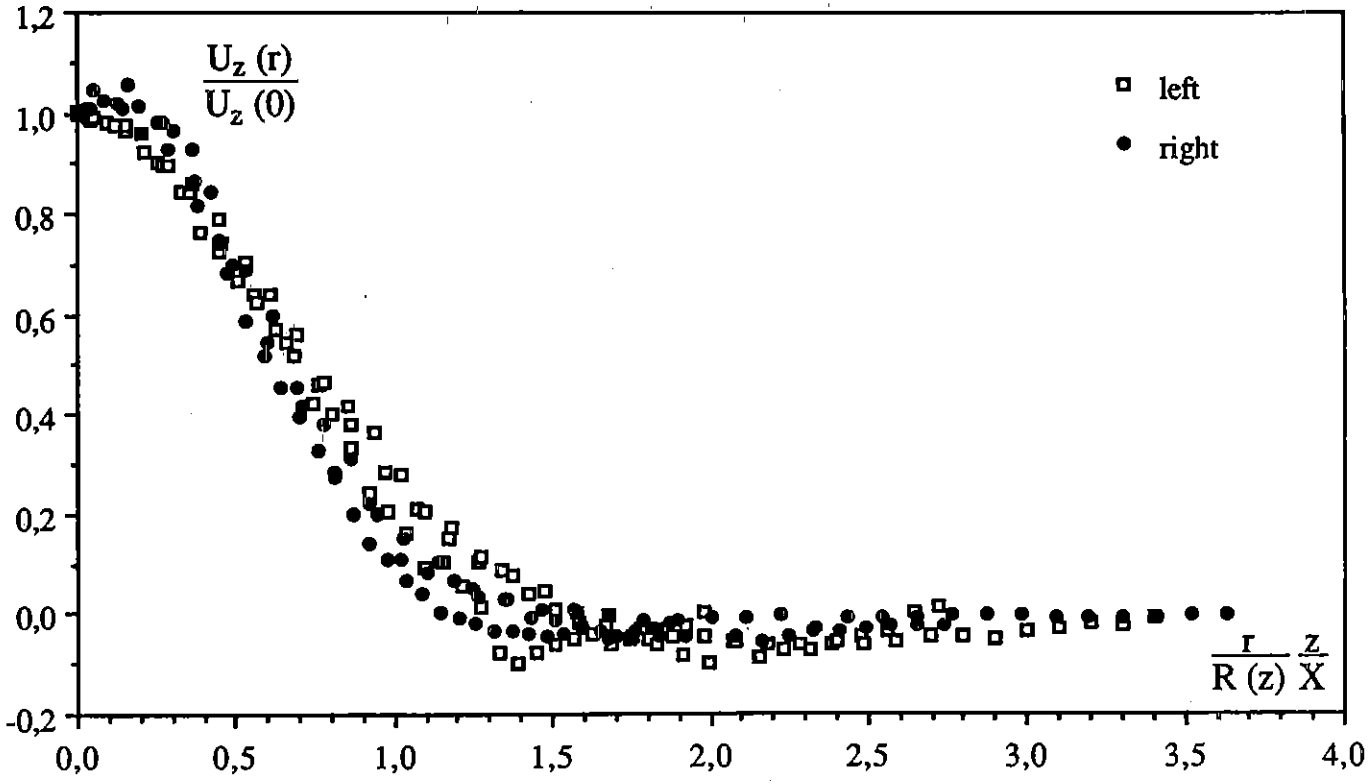

Figure 5.22 : Master curve of the Uz component obtained with the dimensionless parameters

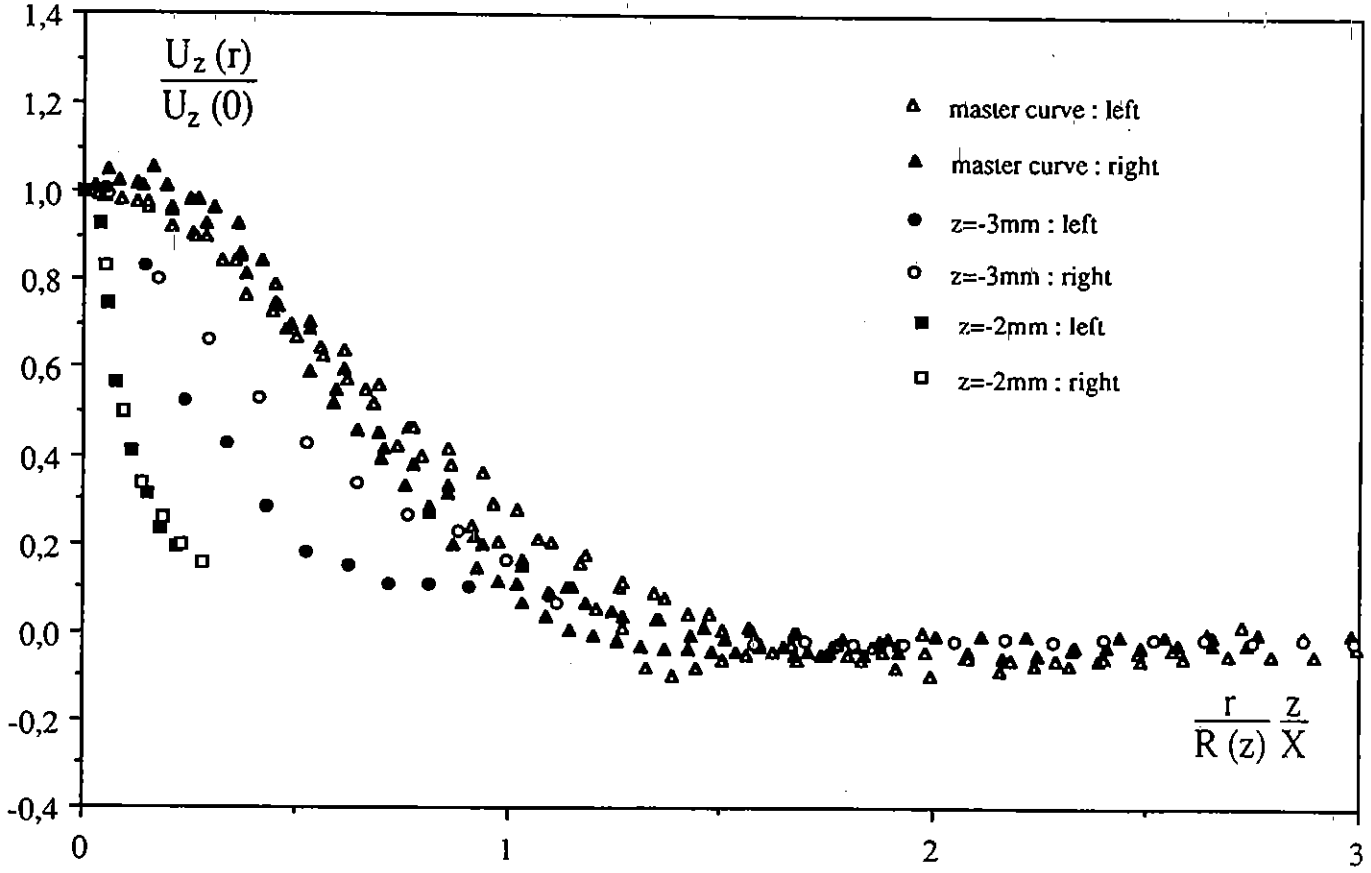

Figure 5.23 : The master curve is not valid in the lower vortex region

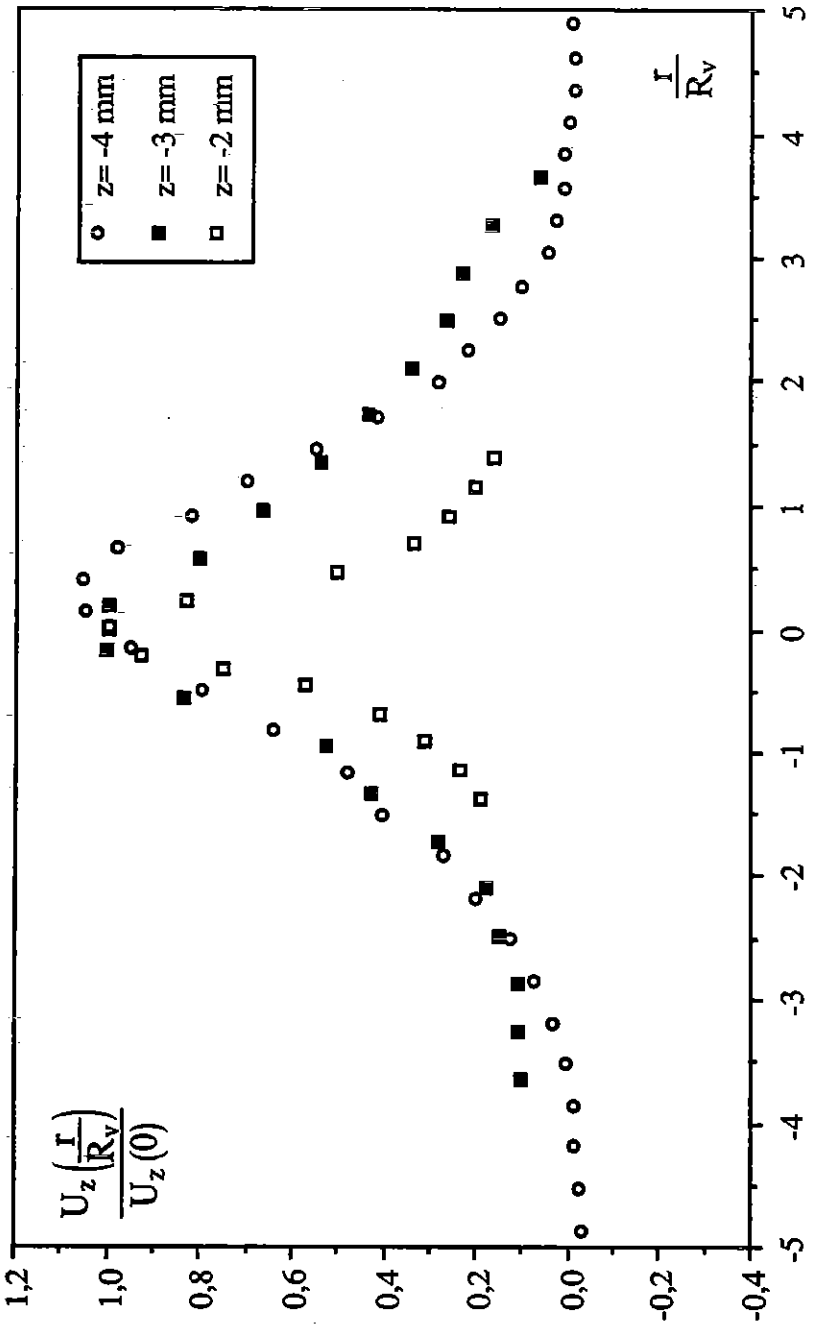

Figure 5.24 : Profiles of the non-dimensionalized vertical component near the orifice